Vortical flow. Part 2. Flow past a sphere in a constant-diameter pipe

By T. W. MATTNER, P. N. JOUBERT and M. S. CHONG

Department of Mechanical and Manufacturing Engineering, University of Melbourne,
Victoria 3010, Australia

This paper describes an experimental and numerical investigation of concentrated vortex flow past a sphere in a constant-diameter pipe. As the swirl was increased at a fixed sphere Reynolds number of approximately 1100, the length of the mean downstream separation bubble decreased. For a small range of swirl intensity, an almost stagnant separation bubble formed on the upstream hemisphere. A further increase in swirl caused the bubble to become unstable and develop into an unsteady spiral disturbance. At very high swirl the downstream separation bubble was eliminated and an unsteady separation zone extended far upstream. Calculations of the vorticity field from surface fits to azimuthal and axial velocity data suggest that upstream separation is caused by the distortion of vortex filaments in the diverging flow approaching the sphere. Numerical solutions of steady inviscid axisymmetric flow past a sphere exhibit a fold in the vicinity of upstream separation. It is suggested that this accounts for the extreme sensitivity encountered in the experiments.

1. Introduction

Interest in vortical flow past a sphere was originally motivated by the classical problem of particle entrainment into turbulent boundary layers. Observations of coherent structures in turbulent boundary layers led Joubert & Wang (1987) to speculate about the role of vortices in the entrainment process. In an effort to understand how vortical structures interact with particles, Joubert & Wang (1987, 1989, 1992) idealized the particle as a sphere and placed it in confined and tornado vortices. A similar fundamental approach to particle-laden turbulent flows was advocated by Kim, Elghobashi & Sirignano (1995) who point out that the standard equation of particle motion is not valid when the eddy and particle are of similar size because the velocity gradients of the carrier flow are no longer negligible. This paper does not address the complex problem of particle entrainment but extends the fundamental work of Joubert & Wang (1987).

We consider the flow of a vortex past a sphere placed on the axis of symmetry of a constant-diameter pipe. The axis of symmetry of the vortex and the pipe are nominally coincident, and the vortex has both azimuthal and axial velocity components (the streamlines are helical). The flow is classified as a streamwise or perpendicular vortex–body interaction by Rockwell (1998). It is related to the classical problem of rotating flow past a sphere originally considered by Proudman (1916) and Taylor (1917), the difference being that the axial vorticity is concentrated in the vortex core. The flow is also related to vortex breakdown. In many studies, breakdown is induced by the adverse pressure gradient (or streamline divergence) due to a flared tube or nozzle.

FIGURE 1. Upstream separation on a sphere. Flow is from top to bottom. Image from unpublished flow visualization by Joubert and Wang.

An adverse pressure gradient (or streamline divergence) is also created by a body placed on the axis of symmetry as the flow approaches the stagnation point. It is widely recognized that objects can strongly affect vortical flows and even provoke breakdown. In particular, Brücker & Althaus (1995) mention the existence of a recirculation region upstream of a hollow hemispherical cap placed in a vortex and comment on its relationship to vortex breakdown. The aim of this study is to examine the changes in flow past a sphere as the swirl intensity is increased from zero with Reynolds number fixed.

Joubert & Wang (1987) investigated the flow of a vortex past a sphere in a pipe for a small range of relatively high swirl intensity. The vortex was generated by a circumferential turning vane arrangement upstream of the working section, which was a constant-diameter pipe. The swirl intensity was characterized by the 'vane swirling angle' and varied from 72° to 84°. The sphere Reynolds number based on the sphere diameter and the bulk axial velocity varied from 388 to 1163. The sphere was mounted on a sting located at two positions on the pipe axis, either upstream or downstream of the sphere. They found that the drag coefficient (based on the bulk axial velocity) was at least an order of magnitude greater than those measured in unswirled flow. The drag coefficient was larger when the downstream sting was used. Flow visualization revealed an unsteady region of separation on the upstream hemisphere and attached flow on the downstream hemisphere, opposite to the flow pattern when the flow is unswirled (figure 1). The separated region extended far upstream and varied in diameter with the sphere size.

Joubert & Wang (1992) subsequently attempted to measure the flow field around the sphere using laser Doppler velocimetry (LDV). In this study, the apparatus was altered so that the swirl was produced by tangential jets prior to entering the working section. Additional unswirled fluid was added through axial jets which were directed onto the free surface of the settling chamber. The sphere was supported by two narrow stings, one upstream and one downstream. Measurements of the flow field failed to provide evidence of upstream separation, which was confirmed by flow

visualization. They found that the upstream sting increased turbulence in the core due to the wake shed from the sting as the vortex core continually shifted position. When the upstream sting was removed, flow visualization again showed the presence of upstream separation. They mentioned that this change of flow structure with sting position was consistent with the change in drag coefficient noted in the earlier study. Panchapakesan *et al.* (1995) subsequently confirmed upstream axial flow reversal using LDV and a downstream sting only.

None of these studies examined the transition from upstream attached flow to upstream separation which must occur as the swirl is increased. The measurements suffered from poor accuracy while the flow exhibited high turbulence levels, significant asymmetry and a curious axial flow regime consisting of an annular region of reverse flow. This flow regime extended through the pipe and was independent of the presence of the sphere.

In preparation for the present study, Mattner, Joubert & Chong (2002) examined the behaviour and properties of the vortex produced by a modified version of the guide-vane-driven apparatus used by Joubert & Wang (1987). These modifications reduced both the turbulence intensity and asymmetry to less than 2% of the bulk axial velocity at zero swirl. For $\beta \leqslant 23°$ (where β is the angle of attack of the guide vane measured at its pivot, as defined in Mattner *et al.* 2002) a steady laminar quasi-cylindrical vortex was established, with properties typical of guide-vane-driven vortex flows appearing in the literature (such properties are summarized by Leibovich 1984 and Escudier 1988). Experiments in this regime (the first three flow cases presented in §4) are therefore free of unusual complicating behaviour and the flow conditions are of general interest. For $\beta \leqslant 23°$, the flow is supercritical, and the effects of downstream boundary conditions are expected to be relatively benign (cf. the effects of downstream boundary conditions in subcritical flow; see Escudier & Keller 1985). Mattner *et al.* (2002) also showed that the annular reverse axial flow regime was the result of a complicated transition process as the swirl intensity was increased following vortex breakdown, which first occurred at $\beta > 23°$. In the present study, the maximum guide vane angle has been limited to $\beta = 39°$ as this avoids the complicating effects of outer-flow unsteadiness and annular axial flow reversal. At this swirl intensity, the flow is subcritical, and it is possible that downstream boundary conditions can have a strong effect on the upstream flow.

Joubert & Wang (1987) did not propose an explanation of upstream separation but compared the separated region to Taylor columns. Brown & Lopez (1990) suggested that the inviscid mechanism responsible for rapid expansion of stream surfaces in axisymmetric vortex breakdown might also be important in vortical flow past solid bodies. This mechanism is also discussed by Althaus, Brücker & Weimer (1995) and Brücker & Althaus (1995), and the latter also mention its importance to vortical flow past an obstacle. Consider flow in a cylindrical coordinate system with radial, azimuthal and axial coordinates (r, θ, z) respectively and corresponding velocity and vorticity components (u, v, w) and (ξ, η, ζ). For inviscid incompressible axisymmetric flow, Brown & Lopez (1990) showed that the azimuthal vorticity depends on the stream surface radius $r = \sigma$ according to

$$\frac{\eta}{\eta_0} = \frac{\sigma_0}{\sigma}\left(\frac{\alpha_0}{\beta_0}\right) - \frac{\sigma}{\sigma_0}\left(\frac{\alpha_0}{\beta_0} - 1\right), \tag{1.1}$$

where $\alpha_0 = v_0/w_0$ and $\beta_0 = \eta_0/\zeta_0$ are the upstream values of the tangents of the helix angles of velocity and vorticity respectively and the subscript 0 denotes values at an upstream station. For $\alpha_0 > \beta_0$, divergence of streamlines ($\sigma/\sigma_0 > 1$) eventually
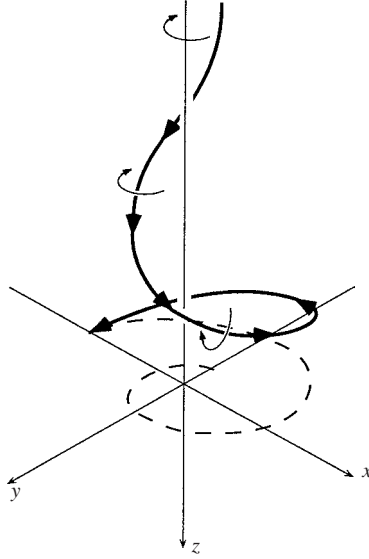
FIGURE 2. Vortex line distortion in rotating, diverging, inviscid flow. Flow direction is top to bottom and the fluid is rotating clockwise when viewed in the positive z-direction. The dashed line is the projection of the vortex line onto the (x, y)-plane.

leads to negative values of η/η_0 for $\eta_0 > 0$. The Biot-Savart law indicates this will reduce the axial velocity near the axis which, through continuity, causes even further divergence of the stream surfaces. Thus for $\alpha_0 > \beta_0$ any initial divergence, such as that caused by a body on the axis or a flared tube, will be amplified, eventually leading to axial flow stagnation. A similar criterion was derived by Rusak (1996). Brown & Lopez (1990) suggested that this positive feedback mechanism may account for axial flow stagnation upstream of a body (upstream separation) as observed by Joubert & Wang (1987).

The change in η is due to distortion of the vortex lines. Figure 2 shows a sketch of a vortex filament in a diverging flow when $\alpha_0 > \beta_0$. The upstream axial velocity w_0 and vorticity ζ_0 are positive, hence the flow circulates in a clockwise direction when looking in the positive z-direction, as can be deduced using the right-hand rule. Consider two particles on a vortex line which is initially almost straight (i.e. β_0 is small). As the flow diverges, moment of momentum is conserved and the azimuthal velocity decreases. The downstream particle will therefore lag behind the trailing particle in the azimuthal direction. The vortex line between the two particles is thus tilted and stretched to form the helical structure shown. The right-hand rule confirms that this deformation results in an axial velocity reduction close to the axis.

The extent to which the above theory can explain the experimental results of Joubert & Wang (1987) is unclear. The upstream flow in the experiment was unsteady, with three-dimensional disturbances and complex right- and left-handed helical vortex lines. In addition, an unpublished video of the flow by Joubert and Wang indicates that there was no upstream station within the test section not affected by the presence of the sphere. In §4, we clarify the application of the theory to upstream separation on the sphere by measuring the velocity field and estimating the vorticity using the methods and analysis described in §2 and §3. In §5, we perform a parametric study of swirling flow past a sphere through a numerical analysis of the Squire–Long equation.
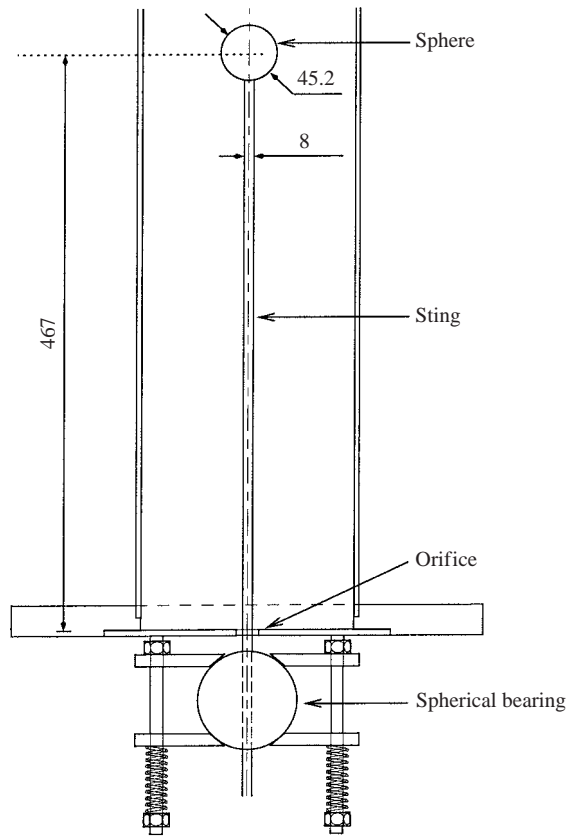
FIGURE 3. General layout of the sphere mechanism showing the sting passing through the centre of the orifice. Flow is from top to bottom. All dimensions in mm.

2. Experimental apparatus and techniques

Apart from the size of the orifice outlet, the apparatus was identical to the one used by Mattner *et al.* (2002) and the reader is referred to that paper for full details. The sphere and its support mechanism are shown in figure 3. The sphere radius r_s was 22.6 mm. The ratio of the sphere radius to the pipe radius R was $r_s/R = 0.263$, resulting in an area blockage of 7%. The sphere was supported by an 8 mm diameter sting which passed out through the orifice and was clamped in an external assembly below the water tunnel. The support assembly allowed the sphere to be located in three dimensions while constraining the downstream end of the sting to remain close to the pipe axis. The orifice diameter was increased from 14.25 mm to 15.8 mm to maintain a similar pipe Reynolds number to Mattner *et al.* (2002), despite the blockage caused by the sting.

Once the sphere was installed, physical access to the working section was impossible. The centre of the pipe was established by firing two laser beams along orthogonal diameters of the pipe. The beams were established on these lines by observing when the incident beam and its reflection from the pipe wall remained in a vertical plane. The sphere position was adjusted until the upstream pole was in the centre of both beams. The uncertainty in locating the sphere at the centre of the pipe using this procedure was approximately ± 2 mm. A horizontal laser beam was used to set the

centre of the sphere 467 ± 0.5 mm above the orifice, close to the middle of the available measurement region.

Laser Doppler velocimetry (LDV) was used to measure the mean azimuthal and axial velocities. Details of the LDV system, the procedures used, and a discussion of the major sources of error may be found in Mattner (2000). Wall approach limitations generally prevented measurements less than 5 mm from the sphere or sting surface, even though these were painted black to maximize visible light absorption. Axial velocity measurements much closer to the sphere were obtained by moving the probe volume off the pipe centreline, so that the optical axis was tangential to the surface. The probe volume was then traversed along the optical axis and the radial position computed from simple geometry (for details, see Mattner 2000). This method also improved the resolution of measurements through the sphere boundary layer, since the traverse was oblique with respect to the direction of the maximum velocity gradient (normal to the wall). Note that the mean flow must be axisymmetric for this technique to work and that this method could not be applied to azimuthal velocities.

Radial traverses were completed at different axial stations. The resolution was increased in regions of high velocity gradient, ranging from 1–5 mm in the radial direction and 2.5–50 mm in the axial direction. As a result, the data do not form a regular grid and in raw form are not amenable to further analysis. Completely regularized splines (Mitásŏvá & Mitáš 1993; Mitásŏvá *et al.* 1995) were used to generate analytic surface fits to the data. The surface $S(\boldsymbol{x})$ is represented by the equation

$$S(\boldsymbol{x}) = \lambda_0 + \sum_{j=1}^{M} \lambda_j R_d\big(\boldsymbol{x}, \boldsymbol{x}^{(j)}\big), \qquad (2.1)$$

where $\boldsymbol{x} = \{x_1, x_2, \ldots, x_d\}$ is an arbitrary point in d-dimensional space, $\boldsymbol{x}^{(j)}$ is the jth discrete data point, $R_d(\boldsymbol{x}, \boldsymbol{x}^{(j)})$ is a radial basis function which is dependent on the dimension d and M is the total number of data points. The coefficients $\{\lambda_0, \lambda_j\}$ are determined by solving the $(M+1) \times (M+1)$ linear system

$$\lambda_0 + \sum_{j=1}^{M} \lambda_j \left[R_d\big(\boldsymbol{x}^{(i)}, \boldsymbol{x}^{(j)}\big) + \delta_{ij} \frac{\omega_0}{\omega_j} \right] = y^{(i)}, \quad i = 1, \ldots, M, \qquad (2.2a)$$

$$\sum_{j=1}^{M} \lambda_j = 0, \qquad (2.2b)$$

where $y^{(i)}$ is the measured quantity at the ith discrete data point and $\delta_{ij} = 1$ when $i = j$ and 0 otherwise. The radial basis functions for explicit values of d are given by Mitásŏvá *et al.* (1995) as functions of

$$\hat{\rho}\big(\boldsymbol{x}, \boldsymbol{x}^{(j)}\big) = \frac{\phi^2}{4} \sum_{i=1}^{d} \big(x_i - x_i^{(j)}\big)^2.$$

This type of spline was chosen as the surface behaviour can be controlled by the smoothing factor ω_0 and the tension parameter ϕ, without requiring data on a regular grid. In the absence of a reliable estimate of individual errors, the weighting factors ω_j were set to unity. Manipulation of ϕ and ω_0 was not sufficient to ensure an adequate fit in the present examples (for a discussion, see Mattner 2000). The physical coordinates were therefore mapped onto the four-dimensional surface defined by

$$x_1 = F(r), \qquad (2.3a)$$

$$x_2 = \alpha_1 z, \tag{2.3b}$$

$$x_3 = G\left((r^2 + z^2)^{1/2} - r_s\right), \tag{2.3c}$$

$$x_4 = \frac{2}{\pi} \tan^{-1}\left(\frac{z}{r}\right), \tag{2.3d}$$

where $F(x)$ and $G(x)$ are stretching functions defined by

$$F(x) = B + \frac{1}{\alpha_2} \sinh^{-1}\left[\left(\frac{x}{x_0} - 1\right)\sinh(\alpha_2 B)\right], \tag{2.4a}$$

where

$$B = \frac{1}{2\alpha_2} \ln\left[\frac{1 + (e^{\alpha_2} - 1)(x_0/x_{max})}{1 + (e^{-\alpha_2} - 1)(x_0/x_{max})}\right], \tag{2.4b}$$

and

$$G(x) = 1 - \frac{\ln\{(\alpha_3 + 1 - x/x_{max})/(\alpha_3 - 1 + x/x_{max})\}}{\ln\{(\alpha_3 + 1)/(\alpha_3 - 1)\}}. \tag{2.5}$$

$F(x)$ stretches the coordinate around the point $x = x_0$, and was used to provide coordinate stretching about the downstream shear layer for $\beta \leqslant 19°$ and about the sting for $\beta = 39°$. $G(x)$ stretches the coordinate around the point $x = 0$ and was used to provide coordinate stretching in the sphere boundary layer. Additional points were added on the sphere and sting surfaces and the corresponding velocity set to zero (no-slip condition), but the surface was not otherwise forced to satisfy any boundary conditions. All dimensions were non-dimensionalized by the pipe radius and all velocities by the bulk axial velocity prior to fitting. A total of five parameters controlled the surface fit: ω_0, ϕ, α_1, α_2 and α_3. The resulting surface was not sensitive to the exact values of these parameters and suitable values were not difficult to find. The appropriate form of the radial basis function for $d = 4$ was

$$R_4\left(x, x^{(j)}\right) = \frac{1 - \exp(-\hat{\rho})}{\hat{\rho}} - 1. \tag{2.6}$$

The spatial derivatives were recovered using the chain rule:

$$\frac{\partial S}{\partial r} = \frac{\partial S}{\partial x_1}\frac{\partial x_1}{\partial r} + \frac{\partial S}{\partial x_2}\frac{\partial x_2}{\partial r} + \frac{\partial S}{\partial x_3}\frac{\partial x_3}{\partial r} + \frac{\partial S}{\partial x_4}\frac{\partial x_4}{\partial r}, \tag{2.7a}$$

$$\frac{\partial S}{\partial z} = \frac{\partial S}{\partial x_1}\frac{\partial x_1}{\partial z} + \frac{\partial S}{\partial x_2}\frac{\partial x_2}{\partial z} + \frac{\partial S}{\partial x_3}\frac{\partial x_3}{\partial z} + \frac{\partial S}{\partial x_4}\frac{\partial x_4}{\partial z}. \tag{2.7b}$$

The component derivatives of equation (2.7) were determined by straightforward analytical differentiation of equations (2.1), (2.3), (2.4) and (2.5).

3. Definitions and flow parameters

3.1. *Coordinate system*

Data are presented in terms of the cylindrical coordinate system and associated velocity and vorticity components defined in §1. The z-axis is coincident with the pipe axis and positive in the bulk flow direction. The origin is located at the centre of the sphere. Capital letters denote the time average.

β (deg.)	Q (m^3 s^{-1})	W_b (m s^{-1})	Γ_0 (m^2 s^{-1})	Ω	Re
0	0.485×10^{-3}	0.0208	0.0	0.0	4291
16	0.485×10^{-3}	0.0208	0.00234	0.65	4291
19	0.485×10^{-3}	0.0208	0.00283	0.79	4291
39	0.484×10^{-3}	0.0208	0.00735	2.05	4192

TABLE 1. Sphere flow parameters.

3.2. Flow parameters

The flow parameters are listed in table 1. The bulk axial velocity W_b is defined in terms of the volume flow rate Q by

$$W_b = \frac{Q}{\pi R^2} \tag{3.1}$$

and the pipe Reynolds number Re by

$$Re = \frac{2W_b R}{\nu}, \tag{3.2}$$

where R is the pipe radius and ν the kinematic viscosity. Note that the sphere Reynolds number Re_s, defined by replacing R with r_s in equation (3.2), is related to the pipe Reynolds number by $Re_s = (r_s/R)Re$ or $0.263Re$ and was therefore fixed at approximately 1100. This does not correspond precisely to a free-stream sphere Reynolds number due to solid blockage effects and the pipe wall boundary layers which make W_b less than the effective free-stream axial velocity. The swirl parameter Ω is defined by

$$\Omega = \frac{\Gamma_0}{2RW_b}, \tag{3.3}$$

where Γ_0 is the circulation at the trailing edge of the guide vanes and is calculated from the guide vane angle β using

$$\Gamma_0 = \frac{Q}{H} \frac{\sin \beta}{\cos \beta - c_{gv}/R_{gv}}, \tag{3.4}$$

where H, c_{gv}, R_{gv} are apparatus-dependent parameters equal to 85 mm, 73 mm and 252 mm respectively. These definitions are consistent with those used by Mattner *et al.* (2002) where the properties of the vacant vortex were established. Note that the pipe Reynolds number in the present experiments is approximately 12% lower. This was due to an 8% decrease in volume flow rate as well as a decrease in equilibrium temperature and consequent increase in viscosity due to cooler ambient temperatures. One consequence of this difference is a change in the value of Ω at which vortex breakdown first appears in the vacant pipe. Figure 15 from Escudier (1988) shows that Γ and Re at vortex breakdown are roughly correlated by $\Omega^3 SRe = $ constant where $S = Q/\Gamma_0 L$, and L is the length of the apparatus. This relationship was originally proposed for a slit-jet-driven vortex flow; however the same figure suggests that data from guide-vane-driven apparatus follow the same trends, at least in a limited Reynolds number range $10^3 < Re < 2 \times 10^4$. For an apparatus with fixed dimensions the correlation reduces to $\Omega^2 Re = $ constant; hence the breakdown swirl intensity Ω_1

at Reynolds number Re_1 is related to that at Re_2 by

$$\frac{\Omega_2}{\Omega_1} = \left(\frac{Re_1}{Re_2}\right)^{1/2}. \tag{3.5}$$

At $Re_1 = 4900$ vortex breakdown appeared when $\Gamma > 0.98$ ($\beta > 23°$, Mattner *et al.* 2002), so for $Re_2 = 4300$ it is expected at $\Omega_2 > 1.05$ ($\beta > 24°$). Based on this correlation, vortex breakdown would not be expected in the vacant flow for the first three cases listed in table 1.

3.3. *Analysis*

In analysing the data, it is assumed that the flow is steady, axisymmetric, and incompressible. Where the flow is unsteady, the data are time averages. In the vacant flow, Mattner *et al.* (2002) found that deviations from axisymmetry were less than 2% of the bulk axial velocity up to approximately $\beta = 45°$. An additional source of asymmetry arises in the sphere experiments due to any eccentricity of the sphere with the vortex or pipe axes. The circulation Γ around the circular path C of radius r was calculated from the surface fits using

$$\Gamma(r) = \oint_C \boldsymbol{U} \cdot \mathrm{d}\boldsymbol{s} = \int_0^{2\pi} rV \, \mathrm{d}\theta = 2\pi rV. \tag{3.6}$$

The stream function ψ defined by

$$U = -\frac{1}{r}\frac{\partial \psi}{\partial z} \quad \text{and} \quad W = \frac{1}{r}\frac{\partial \psi}{\partial r} \tag{3.7}$$

was calculated from

$$\psi(r) = \int_0^r \hat{r} W(\hat{r}) \, \mathrm{d}\hat{r} \tag{3.8}$$

with $\psi(0) = 0$ and $\psi_0 = \psi(R) = Q/2\pi$. The radial velocity U was computed by integrating the continuity equation

$$U = -\frac{1}{r}\int_{r_0}^r \hat{r}\frac{\partial W}{\partial z} \, \mathrm{d}\hat{r}, \tag{3.9}$$

where $U = 0$ at $r = r_0$. The derivative was calculated from the surface fit to W using equation (2.7). The integrals were computed using an adaptive trapezoidal scheme set to give a maximum relative error of 10^{-3}. The three components of vorticity

$$\xi = -\frac{\partial V}{\partial z}, \quad \eta = \frac{\partial U}{\partial z} - \frac{\partial W}{\partial r}, \quad \zeta = \frac{1}{r}\frac{\partial(rV)}{\partial r} \tag{3.10}$$

were calculated by estimating the velocity gradients from surface fits to U, V and W using equation (2.7). At $r = 0$ the axial vorticity was calculated from its limit

$$\lim_{r \to 0} \zeta = 2\frac{\partial V}{\partial r}. \tag{3.11}$$

4. Results

4.1. *Flow visualization*

The flow was visualized by introducing dye from the apex of the contraction, well upstream of the sphere. At $\beta = 0°$ (figure 4a), the flow was steady, laminar, and attached on the upstream hemisphere. Separation occurred downstream of the
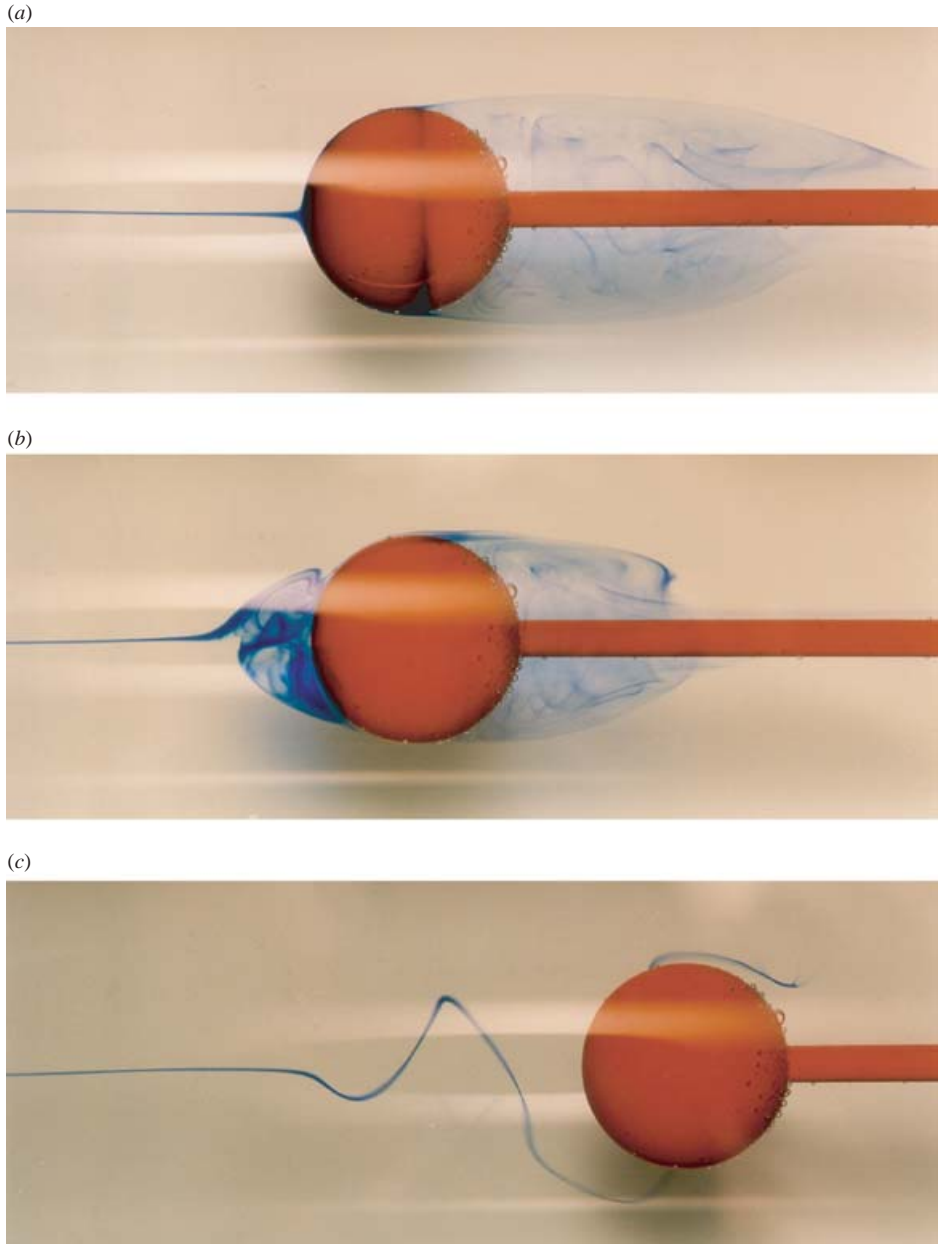
(*a*)

(*b*)

(*c*)

FIGURE 4. Vortical flow past a sphere. Flow is from left to right. (*a*) $\beta = 0°$, (*b*) $\beta = 19°$, (*c*) $\beta = 20°$.

point of maximum thickness, forming a bubble of very slow, reverse axial flow on the downstream hemisphere. The boundary of the bubble was sharply defined and relatively steady up to one diameter downstream of the sphere. Unsteadiness developed further downstream and the rear of the bubble, which was not perfectly closed, was characterized by considerable fluctuations. The flow pattern remained qualitatively similar up to $\beta \approx 17°$. Note that the air bubbles visible in the photographs did not

affect flow field measurements as they disappeared completely during the time allowed for the apparatus to reach thermal equilibrium.

At $\beta = 19°$, a separation bubble appeared on the upstream hemisphere. It was also a region of near-stagnant flow; however the dye in figure 4(*b*) reveals some complicated non-axisymmetric fluid motion in its interior. The bubble was not perfectly steady as occasional puffs of fluid entered near the reattachment point on the sphere. It should be noted that upstream separation occurred at a swirl intensity much less than that required for vortex breakdown in the vacant pipe. There does not appear to have been a great change in the position of the downstream separation point; however the length of the downstream separation bubble (which is better defined in terms of the mean streamlines) appears to have been reduced.

This flow regime appears to have been rather special. Increasing β by as little as 1° caused the bubble to grow in length, become increasingly unsteady and finally develop into the unsteady spiral structure shown in figure 4(*c*). The dye pattern was similar in appearance and behaviour to the spiral disturbance described in Mattner *et al.* (2002). Fluctuations in spiral position and form occurred at a rate which was considerably slower than the rate of rotation. This behaviour made it impracticable to obtain reasonably well-converged data in this regime. The spiral moved upstream with further increase in β, eventually moving into the contraction, leaving an unsteady disordered vortex core in its wake.

4.2. *Mean velocity field*

The flow at zero swirl was measured to establish a datum with which the flows at higher swirl might be compared and to confirm that the flow was free from any unusual behaviour that might have been caused by the boundary conditions or flow quality. The mean velocity distributions are shown in figure 5. The axial flow one diameter upstream of the sphere was uniform except for a 6% deficit near the centre. This is due to the wake shed from the centrepiece in the contraction and was also evident in the absence of the sphere. The azimuthal velocity exhibits a systematic variation close to the upstream pole. The peak azimuthal velocity in this region is as large as 7% of W_b, which is significantly larger than the local axial velocity. Using a potential flow model of the velocity field upstream of the sphere, it can be shown this is consistent with a displacement of the measurement plane from the stagnation point by about 0.9–1.4 mm. This is well within the estimated uncertainty in sphere position. Using the same model, the corresponding error in the axial velocity component is approximately 0.6–1.3% of W_b. Close to the sphere, the axial velocity data from the offset traverse (§2) smoothly overlaps radial traverse data, suggesting that the flow was almost axisymmetric in that region. Near the rear of the separation bubble ($z/r_s \geqslant 3.32$), the overlap was not as smooth, with discontinuities as large as 10–15% of W_b. The offset in this region was not large (being equal to the sting radius) and it is therefore unlikely such a large error was caused by asymmetric mean flow. A more likely explanation is the fluctuation in length (over the five days required for data acquisition) of the separation bubble itself.

The radial gradients associated with the shear layer remain virtually undiminished for approximately one sphere diameter ($0 \leqslant z/r_s \leqslant 2.43$), after which they become smeared. This is consistent with the observation of unsteadiness near the rear of the separation bubble. The time scale of the fluctuations was relatively slow (quasi-periodic with period $1/f \approx 8$–10 s) compared with the limited sample time (120 s) and this contributes to the scatter of the data in this region. Incidentally, this gives a Strouhal number $St = 2fr_s/W_b \approx 0.22$–$0.27$ or, if $1.2W_b$ is used to estimate the
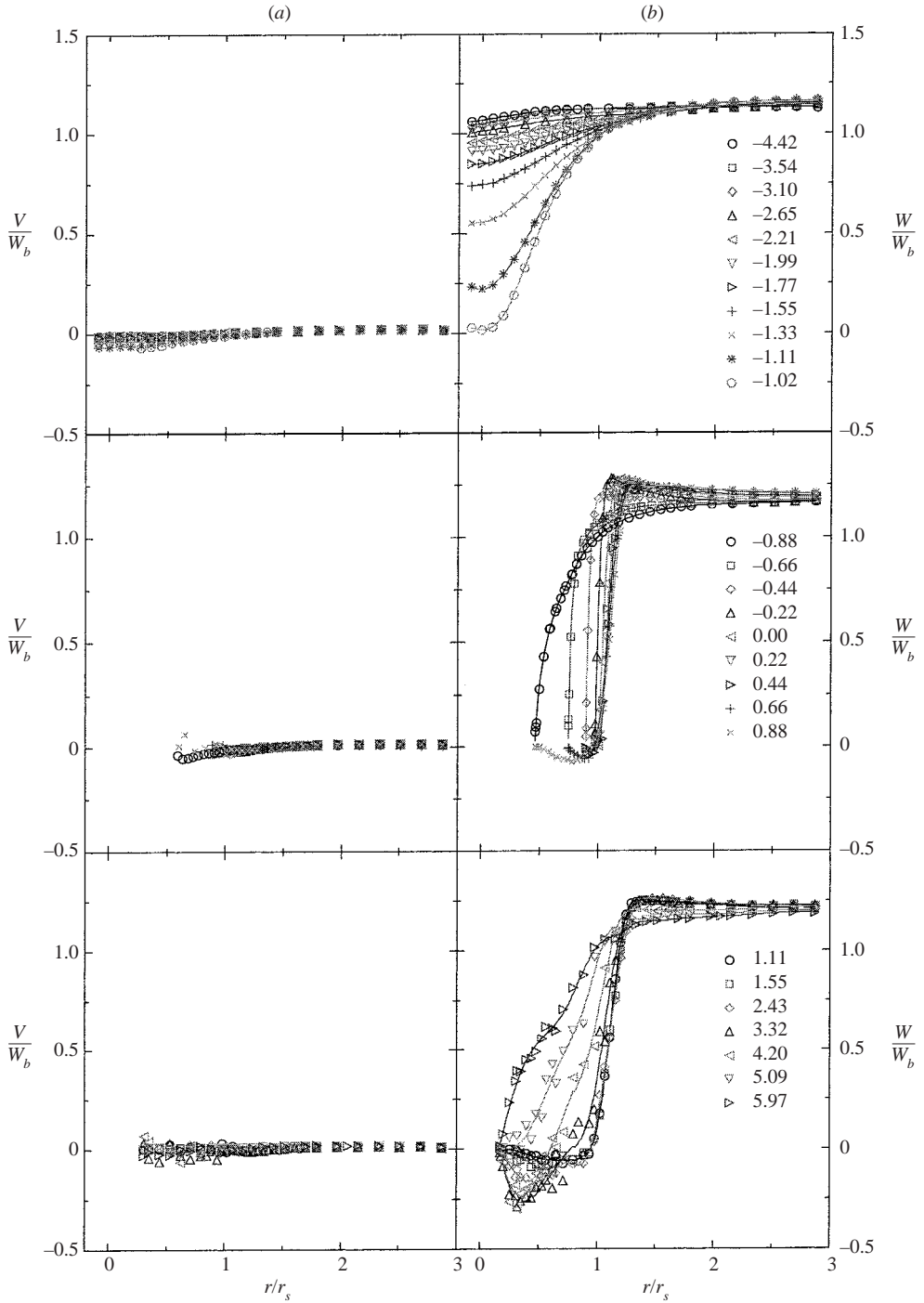
FIGURE 5. Mean azimuthal and axial velocity profiles for $\beta = 0°$, $\Omega = 0$, $Re = 4291$. Solid lines are splines. Legends refer to z/r_s: top figures, $z < -r_s$; middle, $-r_s < z < r_s$; bottom, $z > r_s$.

effective free-stream axial velocity scale, 0.18–0.23. This is in a similar range to values quoted from both experiments and numerical calculations at Reynolds numbers of approximately 1000 (e.g. see Tomboulides & Orszag, 2000).

The flow at $\beta = 16°$ was measured to establish the effects of swirl in the absence of upstream separation. The mean velocity distributions are presented in figure 6. The upstream velocity profiles are similar to those measured by Mattner *et al.* (2002) prior to vortex breakdown. The vortex centreline, defined as the point of zero azimuthal velocity, deviated from the pipe centreline by up to 5% of r_s or 1.3% of R ahead of the sphere. Note that the azimuthal velocity remained non-zero at $z/r_s = -1.11$. It is possible that this is due to the displacement of the measurement plane from the stagnation point, as discussed above. For $r > 2r_s$, the azimuthal velocity was almost unaffected by the presence of the sphere.

Figure 7 shows the mean velocity distributions at $\beta = 19°$. This was the largest value of β to produce an upstream separation bubble sufficiently stable to complete measurements. The separation bubble was a region of slow reverse axial flow and slow azimuthal flow. Note that the disturbance due to the sphere decreases sufficiently far upstream of the sphere and that the axial flow close to the axis of symmetry and downstream of the sphere is reversed (i.e. separated), unlike the flow studied by Joubert & Wang (1987). Furthermore, flow visualization indicates that the bubble is laminar, quasi-steady, and well-defined, again in contrast to the flow observed by Joubert & Wang (1987).

To see if a flow more like that observed by Joubert & Wang (1987) could be obtained, the flow was measured at $\beta = 39°$. At this swirl intensity, vortex breakdown would have occurred and moved up into the contraction even in the absence of the sphere. As a result, the vortex core approaching the sphere was unsteady and this made flow visualization less effective. The mean velocity distributions are presented in figure 8. The mean axial velocity was negative and small in magnitude near the axis as far upstream as measurements could be taken. In the undisturbed flow, the axial velocity profiles were positive, jet-like, and roughly equal to W_b in magnitude (Mattner *et al.* 2002). This indicates that the sphere had a strong and extensive upstream effect on the vortex. In all previous cases the upstream disturbance caused by the sphere died out relatively rapidly. Mattner *et al.* (2002) showed that the flow was supercritical for $\beta \leqslant 23°$ and subcritical at $\beta = 39°$. When the flow is subcritical, it can support upstream-directed infinitesimal axisymmetric waves and downstream disturbances can have large upstream effects (Escudier & Keller 1985). The change in the upstream effect of the sphere is therefore consistent with a change of flow state.

The axial flow was positive downstream of the sphere and accelerated around the downstream hemisphere. The maximum mean azimuthal and axial velocities occurred in a localized region close to the downstream pole of the sphere and the sting. Less than half a diameter downstream of the sphere, both peaks were abruptly destroyed and the subsequent flow developed relatively slowly, if at all, with streamwise distance. It is not known if this abrupt change in velocity is due to sting interference, or is related to the 'vortex jump' observed by Maxworthy (1970) on the downstream hemisphere of a translating sphere in rotating flow.

When β was close to that required to produce an upstream separation bubble, the flow obtained was extremely sensitive and not always unique. It was not possible to stop the apparatus, restart it and continue measurements at a later time, and still maintain precise continuity in the data. All data were therefore collected during a single uninterrupted operation. Part of the problem may have been related to experimental difficulties of the type discussed by Mattner (2000). On the other hand,
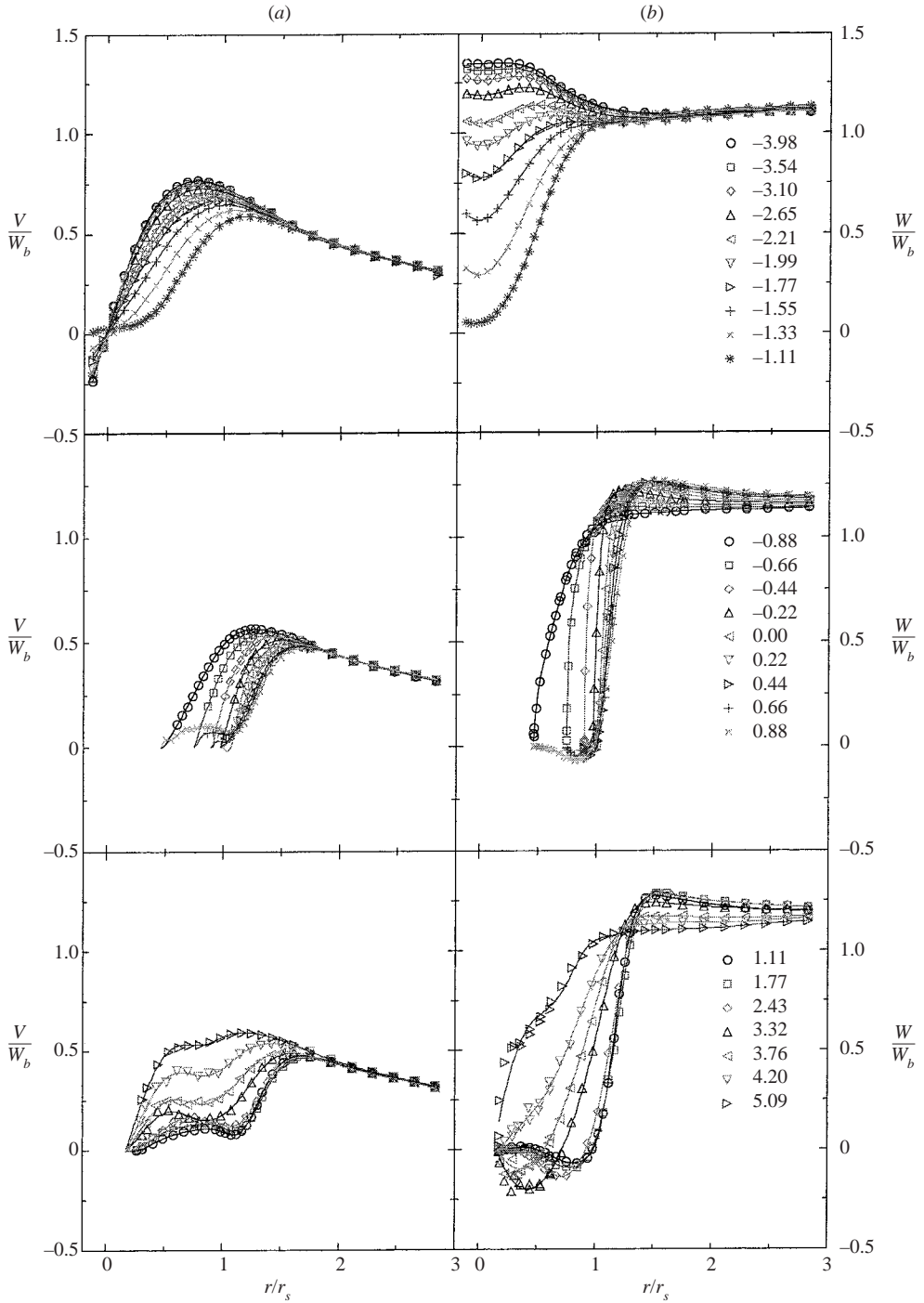
FIGURE 6. As figure 5 but for $\beta = 16°$, $\Omega = 0.65$.

the inherent flow characteristics may also have been a factor. For example, on one occasion when $\beta = 19°$, data were collected showing an unsteady disturbance penetrating up to three diameters ahead of the sphere. This was associated with

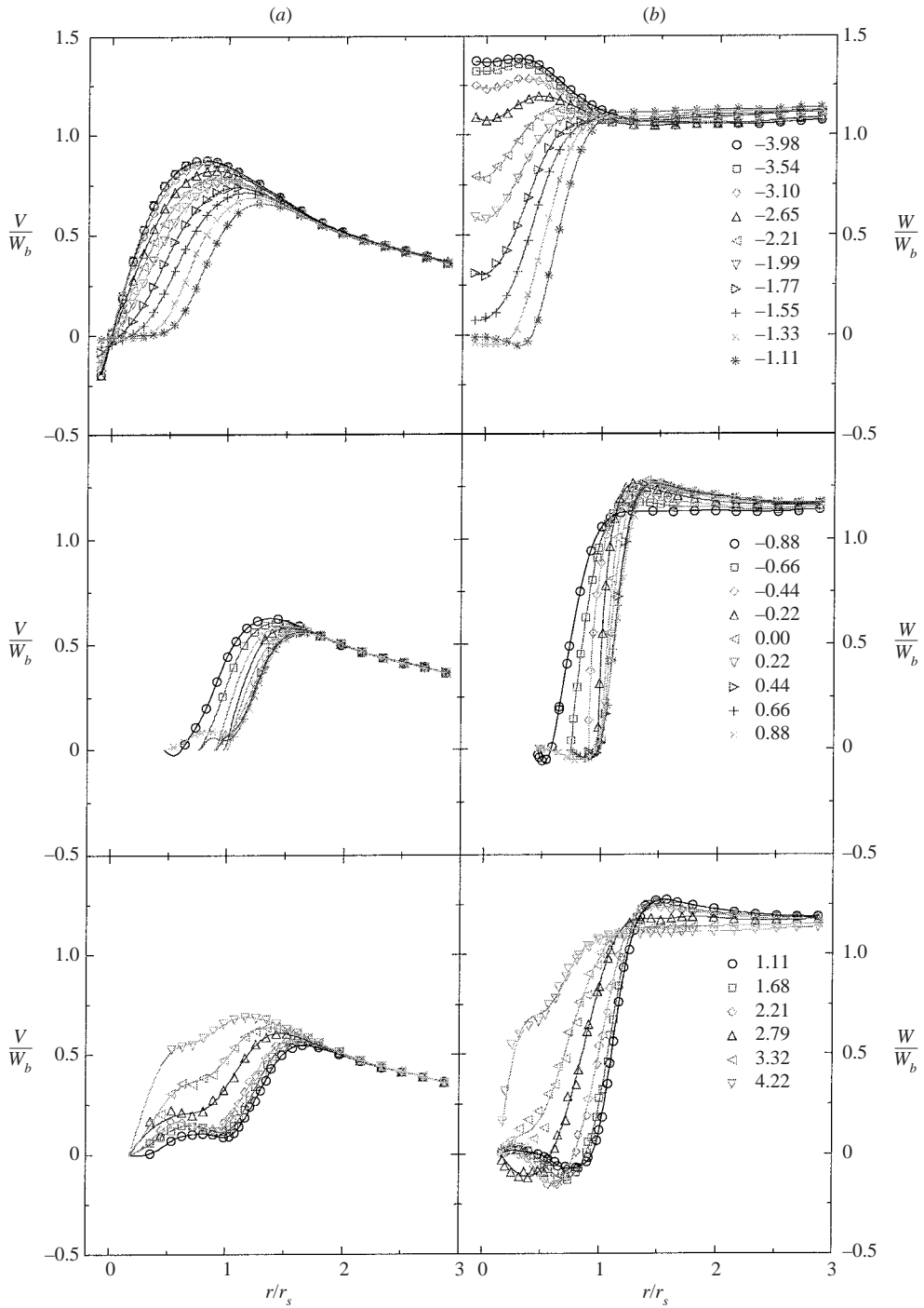(*a*) (*b*)

Legend (upper panels, column b):
- ○ −3.98
- ▫ −3.54
- ◇ −3.10
- △ −2.65
- ◁ −2.21
- ▽ −1.99
- ▷ −1.77
- + −1.55
- × −1.33
- ∗ −1.11

Legend (middle panels):
- ○ −0.88
- ▫ −0.66
- ◇ −0.44
- △ −0.22
- ◁ 0.00
- ▽ 0.22
- ▷ 0.44
- + 0.66
- × 0.88

Legend (lower panels):
- ○ 1.11
- ▫ 1.68
- ◇ 2.21
- △ 2.79
- ◁ 3.32
- ▽ 4.22

FIGURE 7. As figure 5 but for $\beta = 19°$, $\Omega = 0.79$.

the presence of an unsteady spiral structure similar to that shown in figure 4(*c*). This lasted for three days before the flow settled into the steady upstream bubble regime depicted in figures 4(*b*) and 7. At no point was the flow stopped or the flow
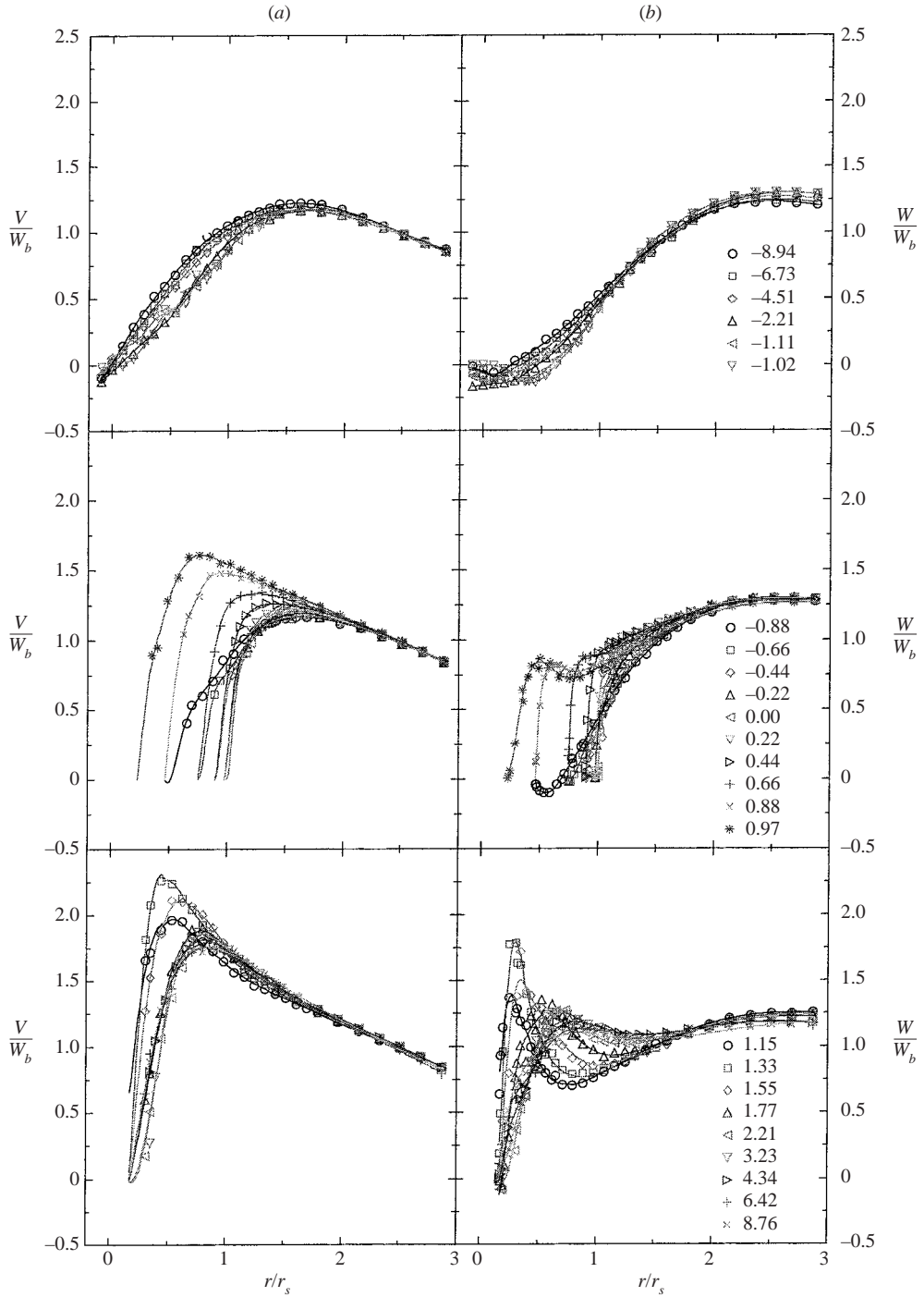
FIGURE 8. As figure 5 but for $\beta = 39°$, $\Omega = 2.05$.

parameters deliberately changed. On another occasion, a steady upstream bubble regime was observed at $\beta = 16°$. This eventually settled into an unseparated upstream flow state over a period of one day. These observations show that dramatic flow

		α_1	α_2	α_3	ϕ	ω_0	*RMS*
$\beta = 0°$	U	0.276	4.0	1.01	20.0	0.0001	8.7×10^{-4}
	V	–	–	–	–	–	–
	W	0.276	4.0	1.01	15.0	0.001	1.8×10^{-2}
$\beta = 16°$	U	0.312	4.0	1.01	20.0	0.0001	4.9×10^{-4}
	V	0.312	4.0	1.01	12.5	0.001	3.6×10^{-3}
	W	0.312	4.0	1.01	12.5	0.001	1.5×10^{-2}
$\beta = 19°$	U	0.341	2.0	1.02	20.0	0.0001	3.6×10^{-4}
	V	0.341	2.0	1.02	15.0	0.001	4.4×10^{-3}
	W	0.341	2.0	1.02	15.0	0.001	1.2×10^{-2}
$\beta = 39°$	U	–	–	–	–	–	–
	V	0.162	3.0	1.01	10.0	0.005	1.8×10^{-2}
	W	0.162	5.0	1.0001	10.0	0.005	3.4×10^{-2}

TABLE 2. Surface fit parameters.

variations can occur even though changes in flow conditions may be very small. This behaviour is discussed in §5.

4.3. *Surface fits*

Table 2 lists the parameters used for surface fitting. Also shown is an estimate of the root-mean-squared error

$$RMS = \frac{1}{M} \sum_{j=1}^{M} \left[y^{(j)} - S(\boldsymbol{x}^{(j)}) \right]^2. \tag{4.1}$$

This is not a completely satisfactory measure of surface quality, since *RMS* could be made as small as desired by increasing ϕ and setting $\omega_0 = 0$. The resulting surface would then include substantial spatial variation between data points. For this reason, figures 5, 6, 7 and 8 show the surface fits at each axial station as solid lines. These figures show that the current technique is able to accurately fit the data where the scatter is small and produces an appropriate 'line of best fit' where the scatter is larger. An example of the spatial distribution of the surface fits is shown in figure 9 for $\beta = 16°$. These can be compared with the original data in figure 10. There is a some waviness evident in the azimuthal velocity fit downstream of the sphere; otherwise the surface fits of the azimuthal and axial velocity components compare well with the original data. The main difficulty is evident adjacent to the upstream pole, where there is a certain degree of discontinuity in the radial velocity. The discontinuity is also evident in the original estimates obtained from the axial velocity surface fit using equation (3.9). It originates from the discontinuity in the boundary condition at the pole ($U = 0$ at $r = 0$ for $z < -r_s$, $U = 0$ on $r^2 = r_s^2 - z^2$ for $-r_s \leqslant z \leqslant r_s$). Either the original data and surface fit are not compatible with this boundary condition (due to the misalignment of the measurement plane with the stagnation point) or the spatial resolution of the data in the axial direction (which affects the estimate of $\partial W/\partial z$ and hence U) is inadequate or there is a combination of both. Note, however, that the same problem was not experienced at $\beta = 19°$ because the flow was almost stagnant in the region surrounding the upstream pole.
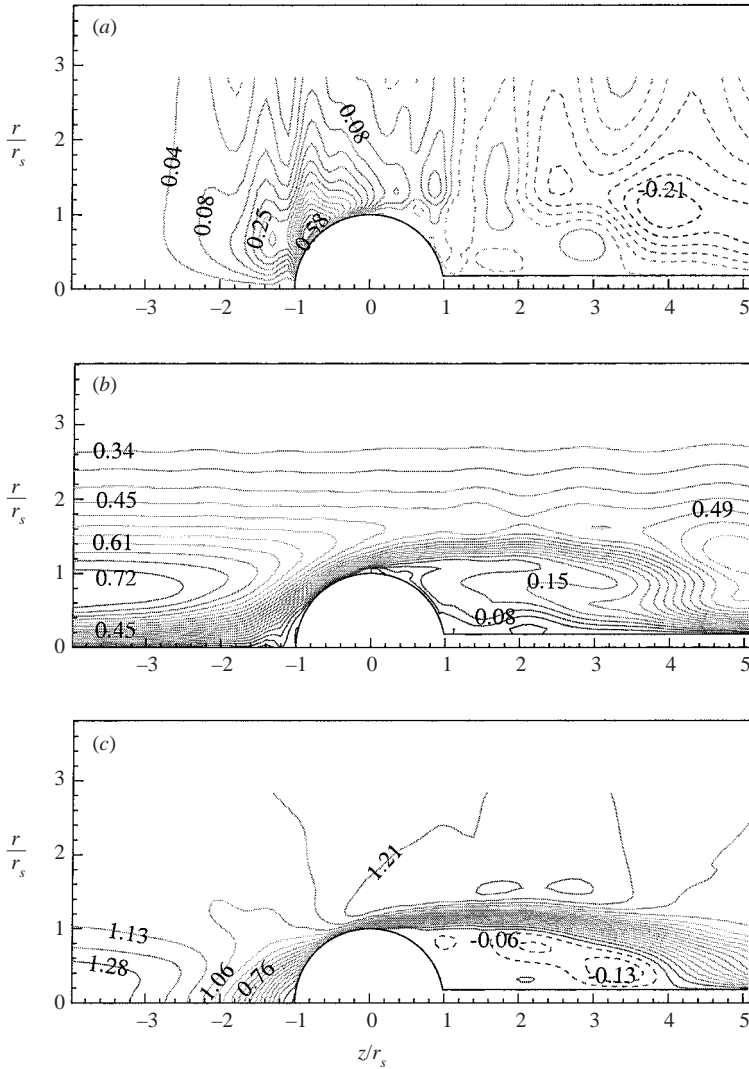
FIGURE 9. Surface fits to (a) U/W_b, (b) V/W_b and (c) W/W_b for $\beta = 16°$. Dashed lines indicate negative velocity. Isoline intervals are: (a) 0.042, (b) 0.038 and (c) 0.075.

4.4. *Circulation and stream function*

Figures 11–13 show the circulation and stream function distributions for the first three flow cases. At $\beta = 0°$, the stream surfaces indicate that the flow separates $102°$ from the upstream pole, forming a mean recirculation bubble approximately 2.1 diameters long. Despite significant blockage effects, a slightly higher Reynolds number and the presence of the sting, these are similar to values obtained by Tomboulides & Orszag (2000) at a Reynolds number of 1000. The rear separation bubble is reduced to 1.6 and 1.1 diameters at $\beta = 16°$ and $19°$ respectively. Evidently, one effect of swirl is to shorten the rear separation bubble.

In steady incompressible inviscid axisymmetric flow, the circulation is conserved on stream surfaces, i.e. $\Gamma = \Gamma(\psi)$. Figure 14 shows Γ plotted versus $(\psi/\psi_0)^{1/2}$, $\psi \geqslant 0$ for (upstream) stations in the range $-3.98 \leqslant z/r_s \leqslant -1.11$. Note that the function
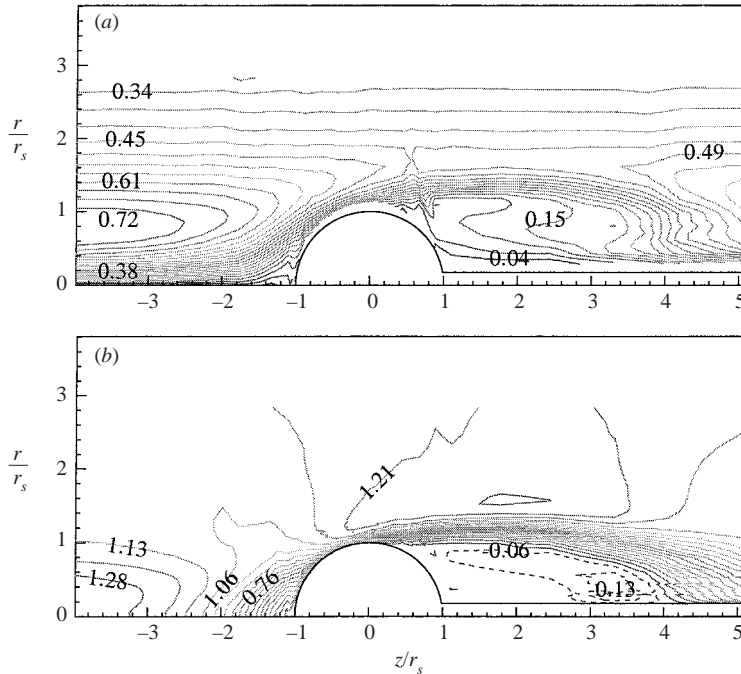
FIGURE 10. (*a*) V/W_b and (*b*) W/W_b for $\beta = 16°$, $\Omega = 0.65$ and $Re = 4291$. Dashed lines indicate negative velocity. Isoline intervals are (*a*) 0.038 and (*b*) 0.075.
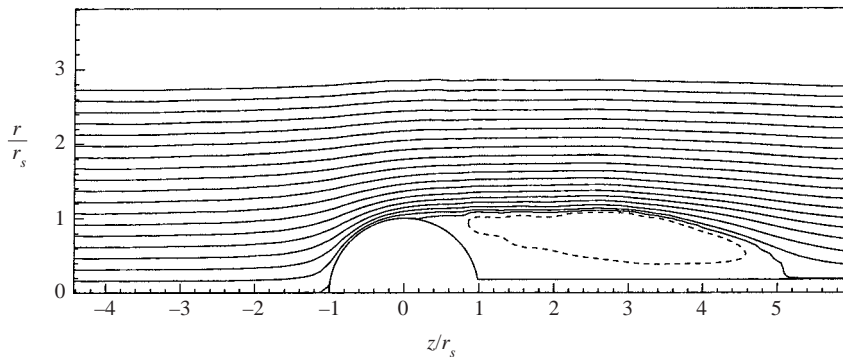

FIGURE 11. Isolines of ψ for $\beta = 0°$.

$(\psi/\psi_0)^{1/2}$ is equal to r/R for uniform axial flow and exposes details near $r = 0$ more clearly than simply plotting versus ψ/ψ_0. The collapse of the data suggests that viscous effects may be neglected in the flow approaching the sphere. This is a local approximation. When viewed at larger scales, the flow develops with streamwise distance as a quasi-cylindrical viscous vortex (Mattner *et al.* 2002). Viscosity influences the flow behaviour by fixing the local flow properties (e.g. peak azimuthal and axial velocities).

An unexpected feature of the circulation distributions at $\beta = 16°$ and $19°$ is the overshoot of Γ_0 by as much as 18% and 11% respectively. Mattner *et al.* (2002) found that Γ exceeded Γ_0 by only 5% for $\beta \leqslant 39°$ and were able to explain that figure in
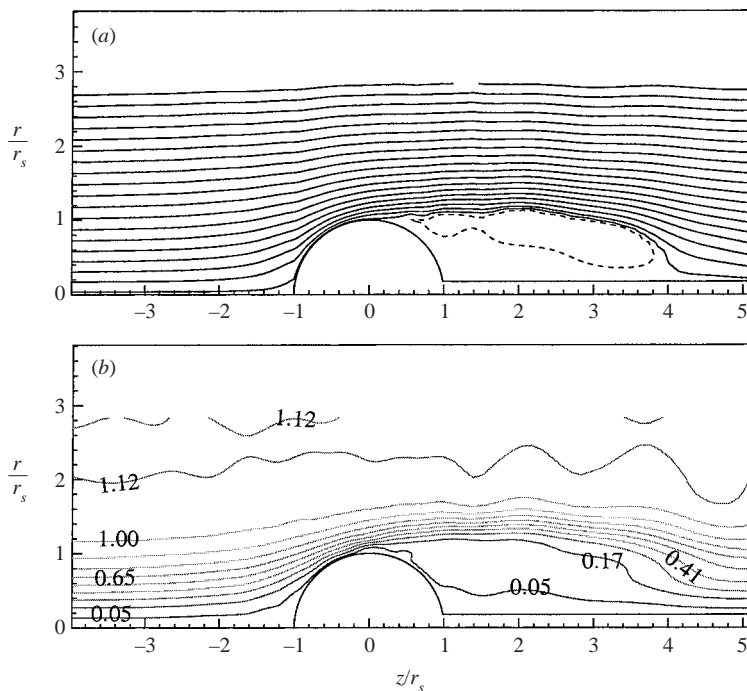
FIGURE 12. Isolines of (*a*) ψ and (*b*) Γ/Γ_0 for $\beta = 16°$. Dashed lines indicate negative values. Isoline interval for (*b*) is 0.12.
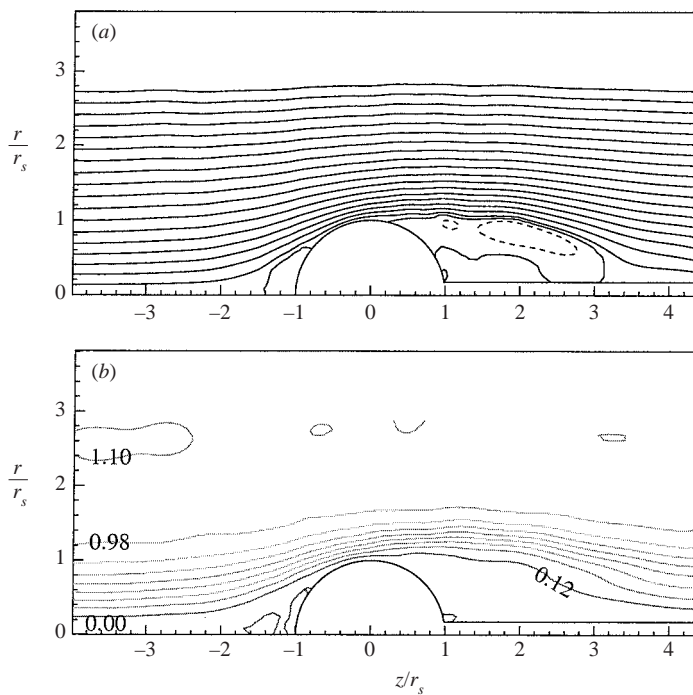
FIGURE 13. Isolines of (*a*) ψ and (*b*) Γ/Γ_0 for $\beta = 19°$. Dashed lines indicate negative values. Isoline interval for (*b*) is 0.12.
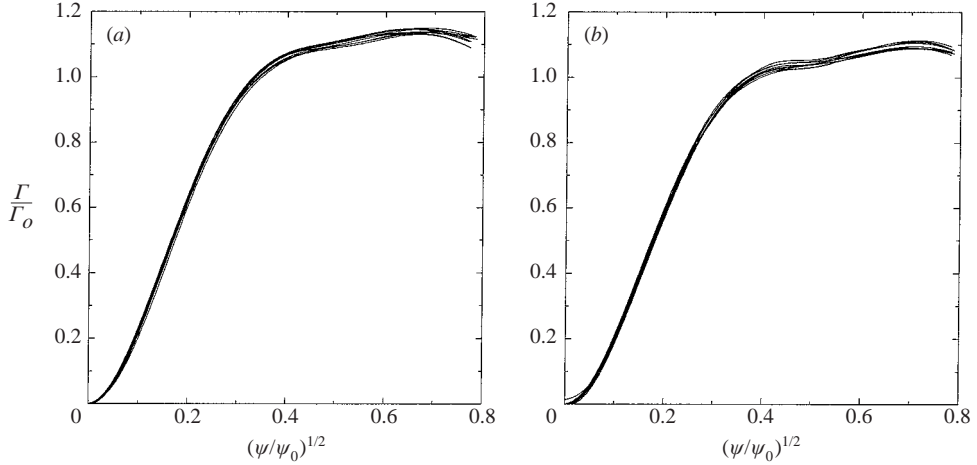
FIGURE 14. $\Gamma(\psi)$ in the range $-3.98 \leqslant z/r_s \leqslant -1.11$ for (a) $\beta = 16°$ and (b) $\beta = 19°$.

terms of the experimental uncertainty or inadequacies in the assumptions leading to equation (3.4). The reason for this inconsistent behaviour is not known; however it is worthwhile pointing out that overshoots are not uncommon. The experimental data of Faler & Leibovich (1978) indicate an overshoot of 38%, while there is an overshoot of 26% in the numerical simulation by Snyder & Spall (2000). Such behaviour makes Ω, as defined by equations (3.3) and (3.4), somewhat unreliable as a flow parameter. If Γ_0 is to be the maximum circulation then the values of Ω in table 1 should be increased to 0.77 and 0.88 for $\beta = 16°$ and $19°$ respectively.

For $\beta = 39°$, figure 15(a) shows an almost stagnant recirculation region extending far upstream of the sphere. It appears that the mean flow shares some of the two-dimensional quality normally associated with Taylor columns in rotating flow. This behaviour has serious implications for numerical or analytical solution of the flow at high swirl, making it difficult to specify the upstream boundary conditions. The flow remains attached on the downstream hemisphere, converging at the downstream pole. Despite the unsteadiness in the core, comparison of figure 15(b) with 15(a) suggests Γ was approximately conserved on stream surfaces, resulting in the large azimuthal velocities near the downstream pole. These features are consistent with the observations of Joubert & Wang (1987). This flow pattern would be consistent with the high-pressure drag coefficients they measured due to the almost stagnant conditions prevailing on the upstream hemisphere (high pressure) and high velocities (low pressure) near the downstream pole. It was not possible to systematically investigate the drag in the current experiments due to the very small hydrodynamic head.

4.5. *Mean vorticity field*

Figure 16 shows the mean azimuthal vorticity for $\beta = 0°$. The other two components are nominally zero and are therefore omitted. Note that all vorticity components have been normalized with respect to r_s and W_b. The plot correctly indicates high negative values of azimuthal vorticity in the attached boundary layer on the upstream hemisphere. The magnitude is reduced in the separated shear layer, initially by viscous diffusion and further downstream by the velocity gradient broadening effects of unsteadiness. There is some positive azimuthal vorticity generated at the sting due to the recirculation in the wake. The qualitative picture is not unlike the instantaneous
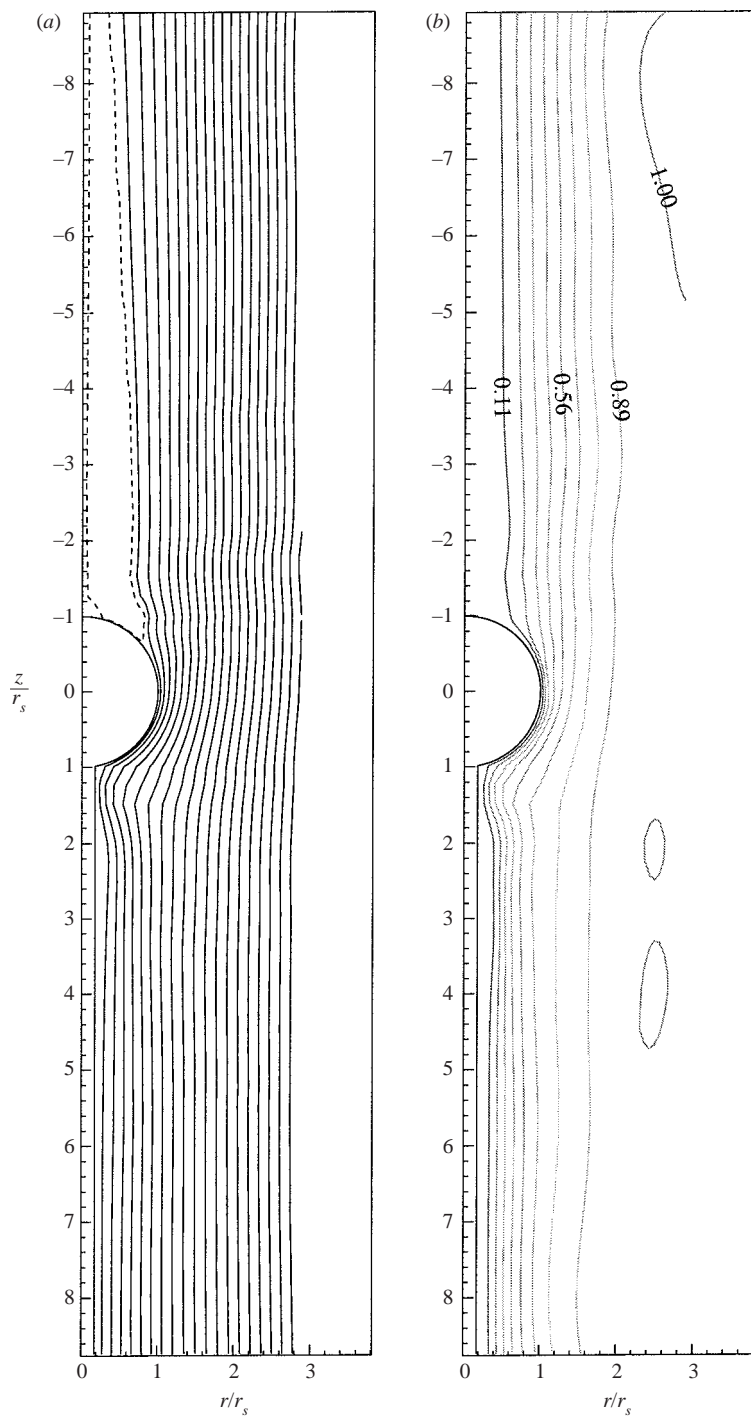
FIGURE 15. Isolines of (*a*) ψ and (*b*) Γ/Γ_0 for $\beta = 39°$. Dashed lines indicate negative values. Isoline interval for (*b*) is 0.11.
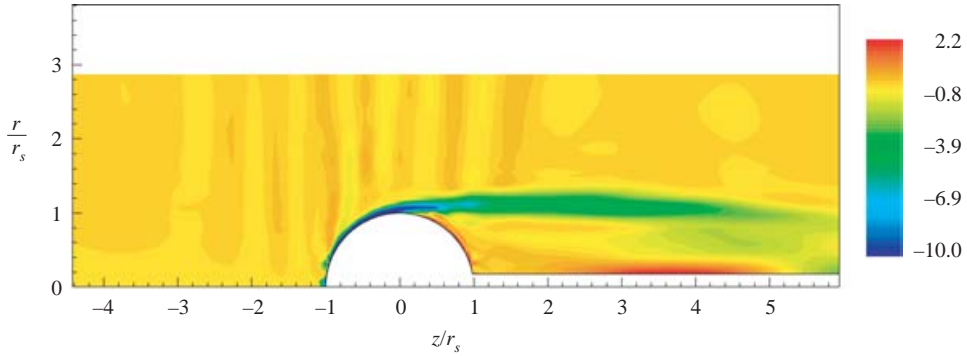
FIGURE 16. $r_s\eta/W_b$ for $\beta = 0°$.

figure 21 from Tomboulides & Orszag (2000); however it is not possible to compare magnitudes as there is no scale given in their diagram. The accuracy of the current estimate of η must be seriously questioned. In addition to assuming axisymmetric flow, the calculations involve taking a derivative of a surface which is itself computed from a derivative determined from experimental (and therefore noisy) data. An estimate of the error involved may be obtained from fluctuations of $r_s\eta/W_b$ in the outer flow. Here the flow should be irrotational, hence the fluctuation of approximately ± 0.5 corresponds to the absolute precision error. Other errors may be significant in regions of high velocity gradient where the vorticity is large. Not only are the measurements subject to errors due to finite probe volume size in these regions, but even small absolute errors in probe volume position will lead to large relative errors in the velocity and hence its gradient. This does not matter greatly as the focus here is on the vorticity upstream of the sphere.

Figures 17 and 18 show all three vorticity components for $\beta = 16°$ and $19°$ respectively. Note that in both cases the incident flow is dominated by the axial vorticity component and that this vorticity is concentrated near the axis. There is also a small positive azimuthal component associated with the axial velocity jet. Using the estimated azimuthal and axial vorticity components and the measured azimuthal and axial velocity components, it is possible to estimate α_0 and β_0 from equation (1.1) and thus verify that $\alpha_0 > \beta_0$ through the vortex core at $z/r_s = -3.98$ in both cases (figure 19). Since the stream function and circulation distributions are consistent with steady axisymmetric inviscid flow (§4.4) and $\alpha_0 > \beta_0$, the positive feedback effect described by Brown & Lopez (1990) (§1) is expected. Figures 17(b) and 18(b) both show a region of negative azimuthal vorticity upstream of the sphere, as predicted by the theory. In the first case ($\beta = 16°$), the results are not convincing due to the positive vorticity adjacent to the upstream pole, which is of similar magnitude to the negative vorticity. This is associated with the discontinuity in the radial velocity distribution at $\beta = 16°$ (as discussed in §4.3). In the second case ($\beta = 19°$), this problem is absent and the minimum non-dimensionalized azimuthal vorticity ahead of the sphere is approximately -3.5. This is significantly larger in magnitude than the estimated uncertainty of ± 0.5. It should be pointed out that, in the inviscid theory, the largest decrease in azimuthal vorticity is not expected ahead of the sphere but close to the equator where σ/σ_0 is a maximum. The generation of negative azimuthal vorticity in the viscous boundary layer on the sphere surface prevents us from observing this. Nevertheless, it appears that the region of negative azimuthal vorticity close to the wall is thicker for $\beta = 19°$ than it is for $0°$.
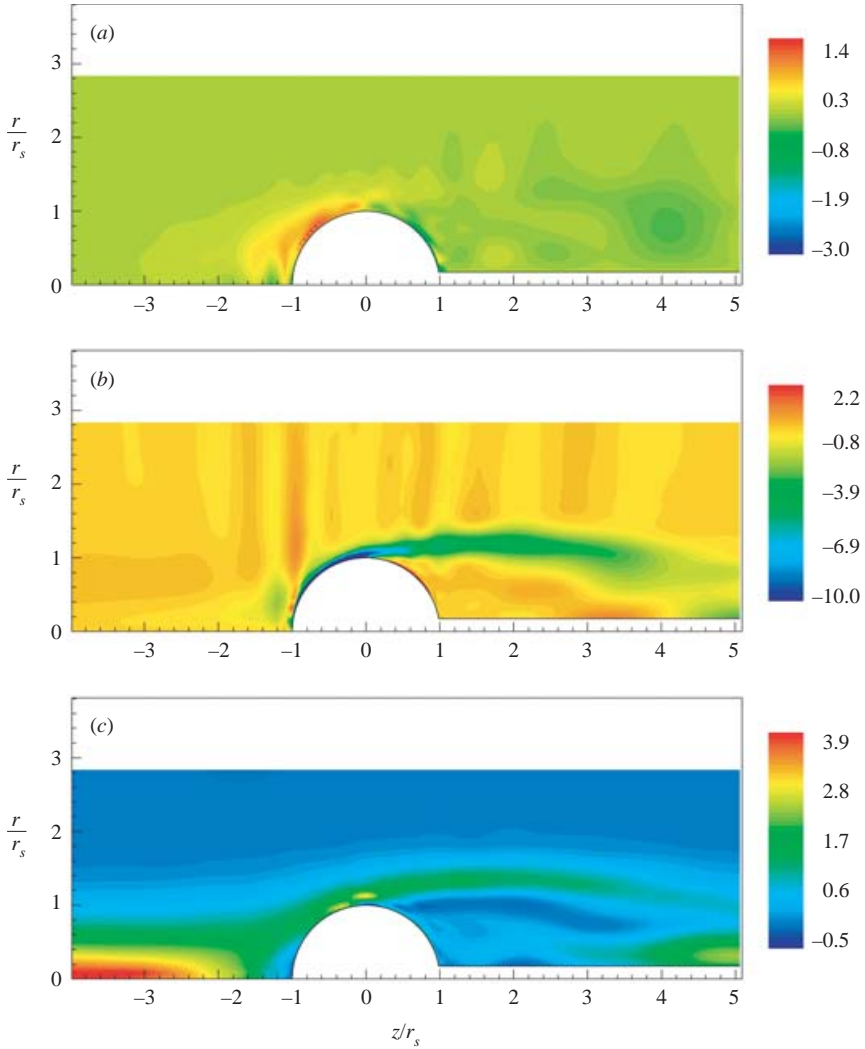
FIGURE 17. (a) $r_s\xi/W_b$, (b) $r_s\eta/W_b$ and (c) $r_s\zeta/W_b$ for $\beta = 16°$.

The remaining two vorticity components also exhibit significant changes ahead of the sphere. The axial vorticity component drops to near zero at the axis. For $\beta = 16°$, this occurs at the upstream pole while for $\beta = 19°$, it occurs at the upstream end of the separation bubble. The axial vorticity maximum is then located at an off-axis point. At the same time, a small positive component of radial vorticity appears. All these variations occur upstream of the sphere. As viscous diffusion is negligible immediately ahead of the sphere and there is no new vorticity being generated in this region, these variations also point to distortion of the vorticity field by the divergent flow approaching the sphere.

The three components of vorticity were integrated to generate vortex lines. Figure 20 shows a perspective view of a single vortex line generated from an initial position $r/r_s = 0.076$, $z/r_s = -3.81$ for $\beta = 19°$. Note that the arrows indicate the direction of the local vorticity vector, while the direction of the induced velocity is determined by the right-hand rule. The calculation was terminated at $z/r_s = -1$ due to the
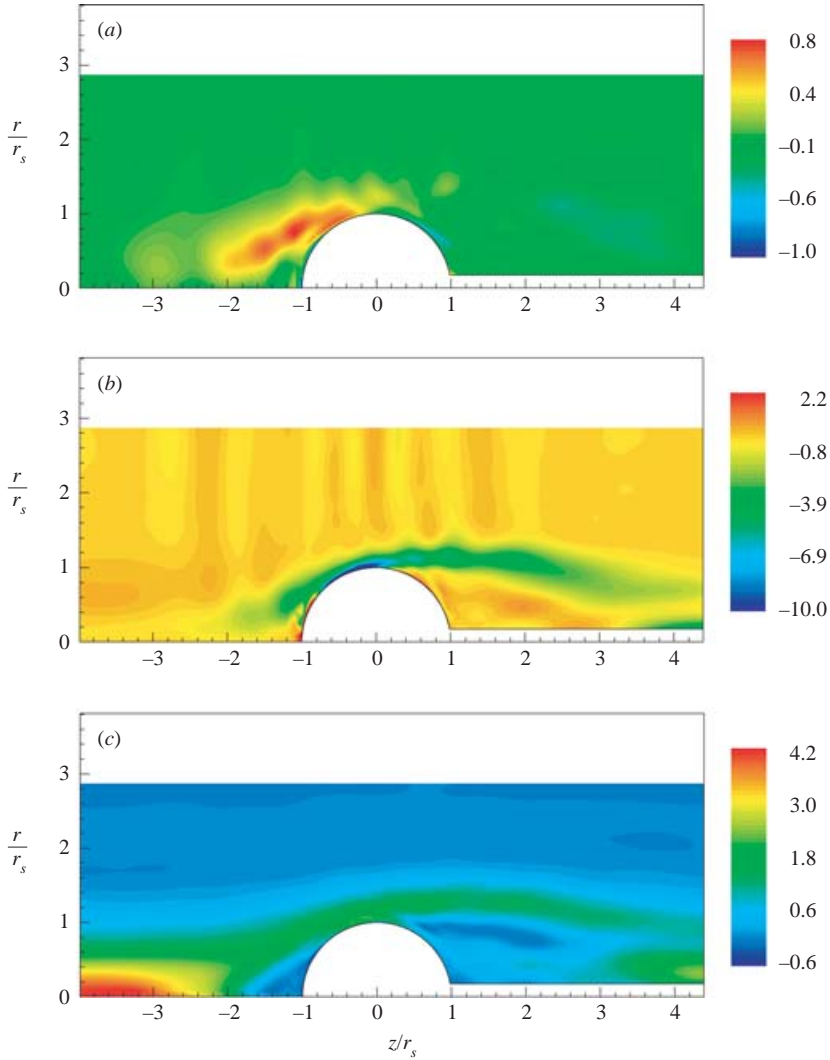
FIGURE 18. (*a*) $r_s\xi/W_b$, (*b*) $r_s\eta/W_b$ and (*c*) $r_s\zeta/W_b$ for $\beta = 19°$.

uncertainty in the radial and axial components of vorticity adjacent to the sphere. Far upstream, the vortex line is almost straight (a helix with a very long pitch) due to the dominance of the axial vorticity. Close to the separation bubble, the vortex line rapidly acquires a helical shape which is consistent with the inviscid deformation process described in §1. Uniqueness conditions on the axis require that the azimuthal and radial components of an axisymmetric flow be zero on the axis. As the axial vorticity also drops to zero at the upstream end of the separation bubble, it follows that there is a critical point in the vorticity field. The form of the vortex lines indicates that it has an unstable focus topology.

Although $\alpha_0 > \beta_0$ is a necessary condition for axial flow stagnation ahead of the sphere (Brown & Lopez 1990), it is not sufficient (Rusak, Whiting & Wang 1998*b*). This is consistent with figure 19, which shows that $\alpha_0 > \beta_0$ for both $\beta = 16°$ and $19°$, even though upstream separation only occurred in the latter case. Axial flow
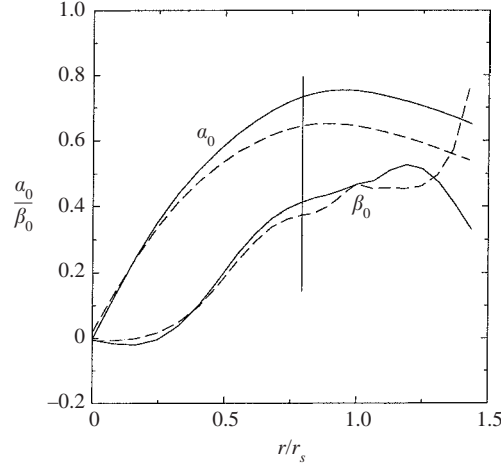
FIGURE 19. α_0 and β_0 for $\beta = 16°$ (dashed lines) and $\beta = 19°$ (solid lines) at $z/r_s = -3.98$. The vertical line indicates the approximate core radius. Note that both η_0 and ζ_0 approach zero in the outer flow, hence the experimental values of $\beta_0 = \eta_0/\zeta_0$ become inaccurate outside the core.
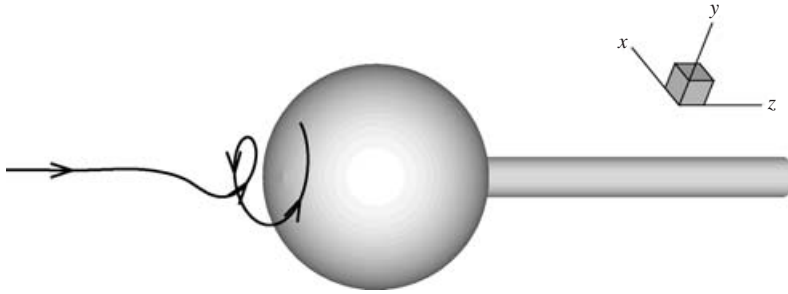

FIGURE 20. A single vortex line upstream of the sphere for $\beta = 19°$.

stagnation is dependent on details of the incident vorticity field and the sphere size. These parameters are systematically investigated in the next section.

5. Steady inviscid axisymmetric flow

5.1. Introduction

For steady inviscid incompressible axisymmetric flow the azimuthal vorticity can be expressed in terms of the stream function ψ by

$$-r\eta = \frac{\partial^2 \psi}{\partial z^2} + \frac{\partial^2 \psi}{\partial r^2} - \frac{1}{r}\frac{\partial \psi}{\partial r} \tag{5.1}$$

and the momentum equations reduce to (see Batchelor 1967)

$$\frac{\partial^2 \psi}{\partial z^2} + \frac{\partial^2 \psi}{\partial r^2} - \frac{1}{r}\frac{\partial \psi}{\partial r} = r^2 \frac{dH}{d\psi} - C\frac{dC}{d\psi}, \tag{5.2}$$

where H is the Bernoulli constant defined by

$$H(\psi) = \tfrac{1}{2}(u^2 + v^2 + w^2) + \frac{p}{\rho} \qquad (5.3)$$

and $C(\psi) = rv$ is proportional to the circulation. Both H and C are constant on stream surfaces. Equation (5.2) has been used in numerous investigations of vortex breakdown and rotating flow past obstacles where it is often referred to as the Bragg–Hawthorne or Squire–Long equation. It is the simplest model incorporating vortex dynamics of the type described in §1. It is interesting to note that solutions of equation (5.2) for rotating flow past obstacles sometimes exhibit upstream separation (Miles 1971). The aim of this section is to examine the nature of the solutions when the flow is a concentrated vortex similar to those in the experiments. The techniques used closely follow those employed by Buntine & Saffman (1995).

The functions $C(\psi)$ and $H(\psi)$ are normally specified from assumed velocity profiles $v(r, z_1)$ and $w(r, z_1)$ at some undisturbed upstream station $z = z_1$. A popular choice is the Q-vortex (Leibovich 1984) given by

$$v = \frac{\omega}{r}\left[1 - \exp\left(-\frac{r^2}{r_0^2}\right)\right], \quad w = W_0 + W_1 \exp\left(-\frac{r^2}{r_0^2}\right), \qquad (5.4)$$

where ω, r_0, W_0 and W_1 are adjustable parameters. This analytically simple model captures the broad features of the undisturbed flow (but not some details, see Mattner *et al.* 2002) and was therefore used in the present study. Integrating the second element of equation (3.7) with respect to r gives $\psi(r, z_1)$ which can be inverted (in this case numerically) to determine $r(\psi, z_1)$ and hence $C(\psi) = r(\psi, z_1)\, v(r(\psi, z_1))$. The function $H(\psi)$ may be determined similarly; however the radial momentum equation must first be integrated with respect to r and then substituted into (5.3) to give

$$H(\psi) = \tfrac{1}{2}(v^2 + w^2) + \int_0^r \left(\frac{v^2}{\hat{r}} - w\frac{\partial u}{\partial z}\right) \mathrm{d}\hat{r}. \qquad (5.5)$$

In calculating $H(\psi)$ it is assumed that $\partial u/\partial z = 0$, which is consistent with undisturbed upstream flow. Equation (5.2) was solved in a domain of length L with the sphere located in the middle. The boundary conditions were

$$\psi(0, z) = 0,\, z^2 > r_s^2, \quad \psi\left((r_s^2 - z^2)^{1/2}, z\right) = 0,\, z^2 \leqslant r_s^2, \qquad (5.6a)$$

$$\psi(R, z) = \frac{Q}{2\pi} = \psi_{-L/2}(R), \qquad (5.6b)$$

$$\psi(r, -L/2) = \psi_{-L/2}(r), \qquad (5.6c)$$

$$\frac{\partial \psi}{\partial z}(r, L/2) = 0, \qquad (5.6d)$$

where $\psi_{-L/2}$ denotes the stream function determined from the inlet axial velocity profile. The outlet boundary condition (5.6d) was used by Wang & Rusak (1997b) and Rusak, Wang & Whiting (1998a) in their theory and numerical simulations of inviscid vortex breakdown in a pipe. It is not completely consistent with the physical flow, where the orifice outlet acts like a sink on the axis, but the experiments suggest that (in the mean) $\partial \psi/\partial z$ becomes small at some point between the sphere and the orifice. In any case, the inviscid model cannot accurately reproduce the physical flow downstream of the sphere, as boundary layer separation and wake formation are impossible without the inclusion of viscosity.
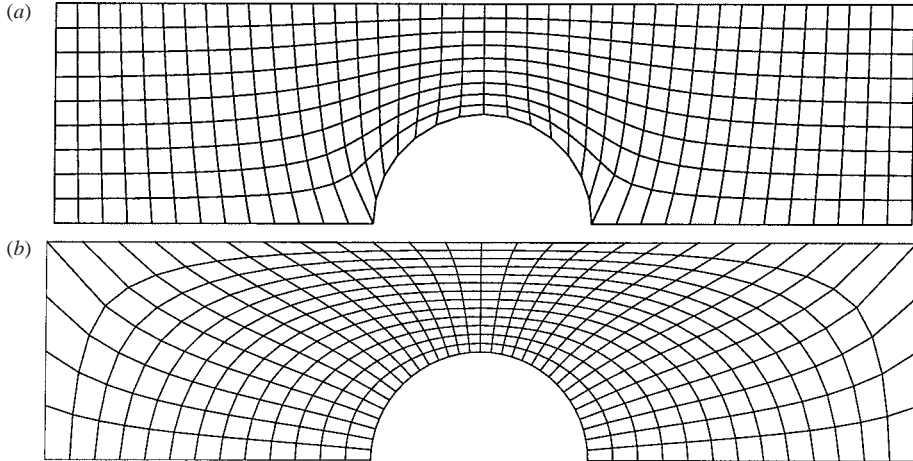
FIGURE 21. Example grids for $L = 4$ and $r_s = 0.5$: (a) A-grid, 10×41, and (b) B-grid, 14×33. Note that the grids shown are much coarser than the grids used in the calculations, and are for illustrative purposes.

Coordinate transformation techniques were used to map the sphere and pipe geometry and the governing equation (5.2) onto a rectangular domain. An elliptic grid generator was used to construct two types of mesh (referred to as A- and B-grids), examples of which are shown in figure 21. The problem was discretized using standard second-order-accurate central finite differences and the resulting nonlinear equations solved using the Newton–Raphson method. Pseudo-arclength continuation (e.g. Beran & Culick 1992) was used to trace the solution paths.

Second-order accuracy of the numerical solution was verified by solving the problem of unbounded potential flow on different resolution grids (from 10×41 to 90×361 for A-grids and 50×100 to 200×400 for B-grids) and computing the truncation error from the analytic solution. Rotating flow past a sphere in a pipe was solved on a 30×121 A-grid with aspect ratio $L/R = 4$, and on a 30×361 A-grid with $L/R = 11.5$, both with $r_s/L = 0.25$. When the flow was subcritical, standing waves formed throughout the domain. The amplitude and phase of these waves was strongly dependent on the aspect ratio. Wavelengths estimated from the numerical solutions were within 1% of the exact wavelength obtained from linear theory (Long 1953). In subcritical flow, the boundary conditions used here are unable to impose the condition of no upstream influence (for a more complete discussion, see Mattner 2000). When the swirl intensity was decreased below critical, the effect of aspect ratio progressively weakened. For the Q-vortex results presented in § 5.2, the flow conditions are always supercritical and we expect $L/R = 4$ to be adequate. The effect of aspect ratio on the Q-vortex results was checked at $r_0/R = 0.15$, $W_2/W_1 = 1.25$ and $\Omega = 1.005$ using the same A-grids as the rotating flow. Differences in the scaled azimuthal vorticity were less than 1%. The effect of grid resolution was studied using a 60×241 A-grid under the same flow conditions (which correspond to the steepest velocity gradients examined in this study). Differences in the scaled azimuthal vorticity were less than 3%. For the A-grids, a discontinuity in the metrics caused the largest relative error to be located near the poles of the sphere. For the B-grids, this discontinuity was shifted to the junction of the wall and the inlet and outlet boundaries. Consequently, quantities such as the axial velocity gradient $\partial w/\partial z$ at the poles could be calculated more accurately

on B-grids than A-grids. For this reason, B-grids were used to generate all the data presented in §5.2, but the entire set of calculations was duplicated on A-grids. Two solutions were compared at $r_0/R = 0.15$, $W_2/W_1 = 1.25$ and $\Omega = 0$ using a 30×121 A-grid and a 100×200 B-grid. Differences in the scaled azimuthal vorticity were less than 2%. The accuracy of computing $\partial w/\partial z$ at the sphere poles was checked on a 100×200 B-grid by solving the unbounded potential flow problem. The error was less than 1%. For a Q-vortex with $r_0/R = 0.15$, $W_2/W_1 = 1.25$ and $\Omega = 0$, increasing the resolution of the B-grid from 100×200 to 200×400 changed $\partial w/\partial z$ at the sphere poles by less than 1%. Using the result obtained on the B-grid as a reference, the maximum error in estimating $\partial w/\partial z$ from a 30×121 A-grid for the entire parameter range was 10%. The parameters Ω_0 and Ω_f (defined in §5.2) were also computed for both grid types and each differed by less than 5% over the entire parameter range.

5.2. *Results*

For this section, the swirl parameter Ω is redefined as

$$\Omega = \frac{2\pi\omega}{2RW_0}, \tag{5.7}$$

where ω and W_0 are taken from the Q-vortex definition given in equation (5.4). For values of r_0/R and W_1/W_0 typical of the experiments, $2\pi\omega \approx \Gamma_0$ and $W_0 \approx W_b$ hence this redefinition is roughly comparable to the swirl parameter used in the experiments. To illustrate the solution path in a two-dimensional diagram, it is also necessary to introduce a relevant scalar function of the solution. For example, studies of vortex breakdown often use the minimum axial velocity on the axis (Beran & Culick 1992; Buntine & Saffman 1995; Wang & Rusak 1997a). This choice is not suitable in the present case because, until upstream separation occurs, the minimum axial velocity is always zero on the sphere poles. Upstream separation on the sphere can be detected by monitoring the value of

$$-\frac{\partial w}{\partial z}\bigg|_{(0,-r_s)} = -\frac{1}{r}\frac{\partial^2\psi}{\partial z\partial r}\bigg|_{(0,-r_s)}$$

at the upstream pole where $(r, z) = (0, -r_s)$. This parameter is positive if the axial flow immediately upstream of the sphere is positive (and therefore decreasing with axial distance approaching the stagnation point at the pole) and vice versa.

The solution behaviour for two sphere sizes, $r_s/R = 0.25$ and 0.35, over a parameter range $0.15 \leqslant r_0/R \leqslant 0.40$ and $0 \leqslant W_1/W_0 \leqslant 1.25$ was investigated. Solutions shown here were obtained on a 100×200 B-grid with $L/R = 4.0$. Figure 22 shows solution paths for $r_s/R = 0.25$ only. For the range of parameters investigated, it was nearly always possible to arrive at a swirl intensity Ω_0 where the solution exhibits upstream separation, that is, $-\partial w/\partial z < 0$. Flow reversal near the axis is associated with negative values of ψ (see figure 24h), but the functions $C(\psi)$ and $H(\psi)$ are only strictly specified for $0 \leqslant \psi \leqslant Q/2\pi$. Additional boundary conditions are required to specify the flow outside this range. In the present study, analytic continuation of $C(\psi)$ and $H(\psi)$ into $\psi < 0$ was used. Although mathematically valid, the physical validity of this procedure has been discussed at some length in the literature (Leibovich 1984; Leibovich & Kribus 1990). Ideally, the separated region would be treated as a stagnation zone since Rusak *et al.* (1998a) have shown this to be consistent with the asymptotic behaviour of the unsteady axisymmetric Euler equations. To implement this properly, it is necessary to determine the location of the $\psi = 0$ stream surface by balancing the internal and external pressure. This type of free-surface problem is
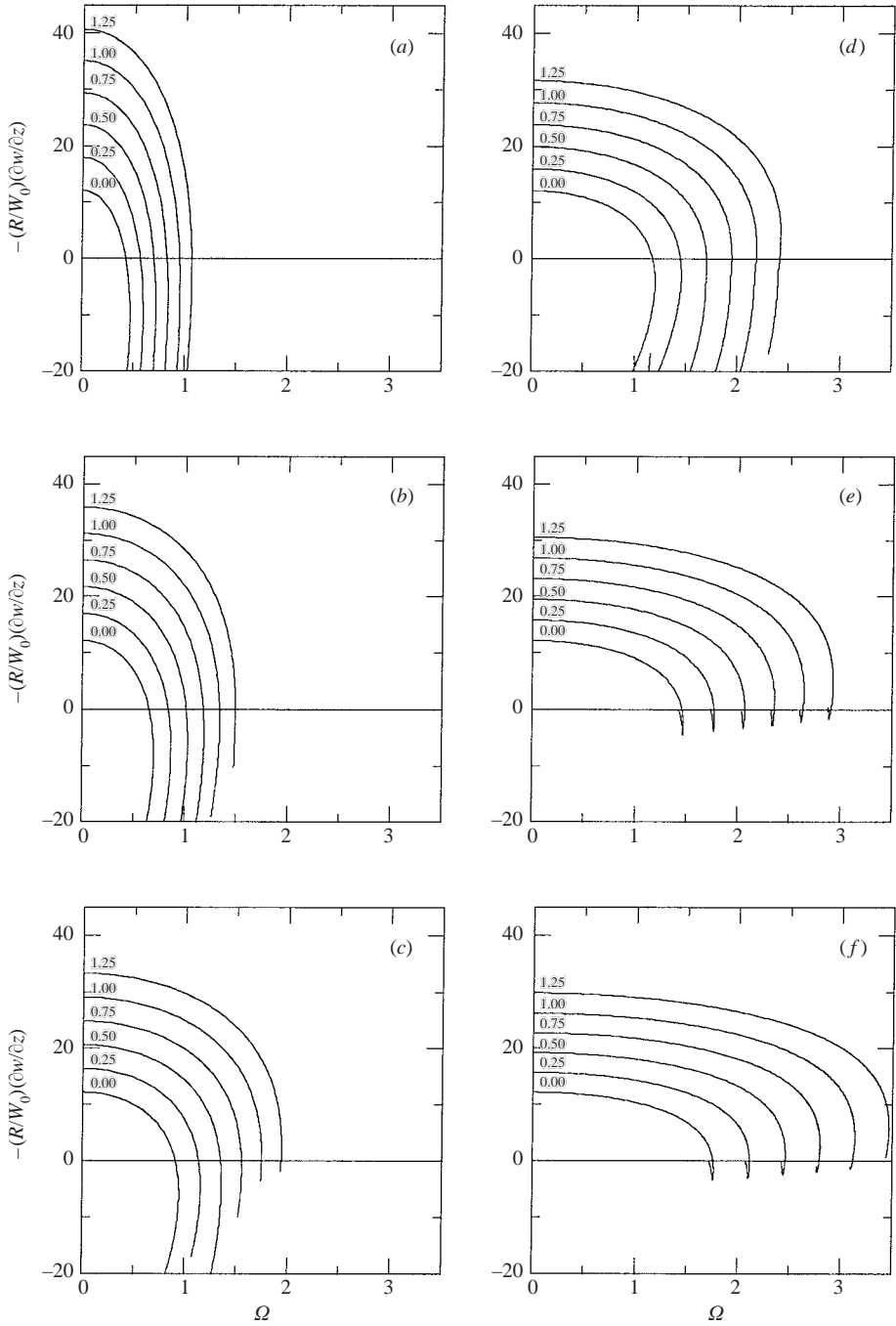
FIGURE 22. Solution paths for $r_s/R = 0.25$. The labels refer to the value of W_1/W_0 on each path. The solid horizontal line indicates when upstream separation occurs. $r_0/R = $ (*a*) 0.15, (*b*) 0.20, (*c*) 0.25, (*d*) 0.30, (*e*) 0.35, (*f*) 0.40.
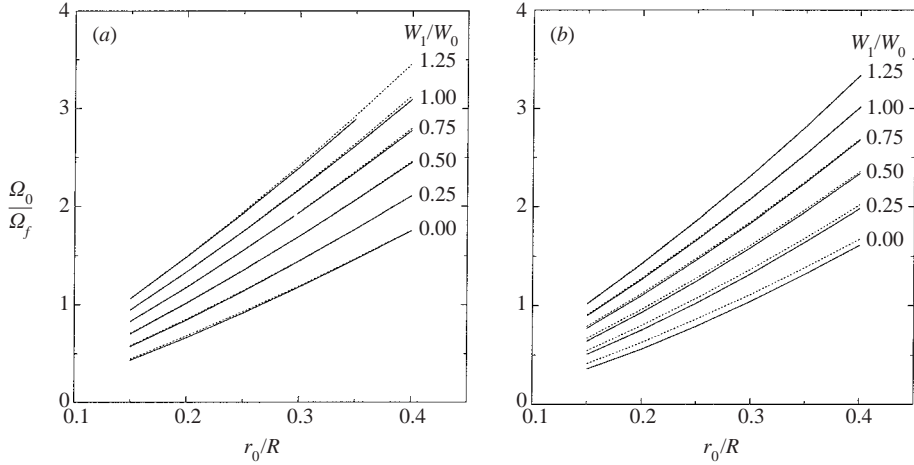
FIGURE 23. Critical swirl intensities for (a) $r_s/R = 0.25$ and (b) $r_s/R = 0.35$. The solid lines refer to Ω_0 and the dotted lines to Ω_f.

outside the scope of the present calculations. This limitation does not however affect the study of the onset of separation or the associated physical mechanisms.

A limit point, or fold, (where Ω reaches a local maximum, Ω_f) was always encountered at some stage of the continuation. Buntine & Saffman (1995) and Rusak, Judd & Wang (1997) previously observed folding of solutions to the Squire–Long equation for swirling flow through diverging pipes. Here, Ω_0 was extracted from the solution paths using linear interpolation, while Ω_f was simply taken as the maximum discrete value of Ω. The results for both sphere sizes are summarized in figure 23. Upstream separation and folding occurred very close together, i.e. $\Omega_0 \approx \Omega_f$. Inspection of the solution paths reveals that, at low values of W_1/W_0, upstream separation preceded folding while the opposite was true at larger values of W_1/W_0. Increasing core size r_0 delayed upstream separation (i.e. increased Ω_0), as did a stronger axial velocity jet (larger W_1/W_0), while increasing sphere size r_s decreased Ω_0. These results may be explained in terms of the ratio α_0/β_0. For a Q-vortex,

$$\frac{\alpha_0}{\beta_0} = \left(\frac{\omega}{RW_0}\right)^2 \frac{1 - \exp\left(-\hat{r}^2/\hat{r_0}^2\right)}{(W_1/W_0)\left[1 + (W_1/W_0)\exp\left(-\hat{r}^2/\hat{r_0}^2\right)\right]} \frac{1}{\hat{r}^2}, \qquad (5.8)$$

where $\hat{r} = r/R$ and $\hat{r_0} = r_0/R$. Note that the factor ω/RW_0 is directly proportional to Ω. If W_1/W_0 is increased with all other parameters held fixed, α_0/β_0 is reduced. For a fixed streamline divergence $\sigma/\sigma_0 > 1$ this will increase the azimuthal vorticity, thereby increasing the axial velocity induced at the centreline and delaying axial flow stagnation. Increasing r_0/R with all other parameters held fixed reduces the numerator and increases the denominator so that α_0/β_0 is once again reduced and the same consequences follow. Increasing r_s/R increases the peak streamline divergence which, provided $\alpha_0 > \beta_0$, decreases the azimuthal vorticity, further retarding the axial flow induced at the centreline and causing axial flow stagnation to occur earlier.

Figures 24 and 25 show the stream function and azimuthal vorticity for several values of Ω with $r_s/R = 0.25$, $r_0/R = 0.20$ and $W_1/W_0 = 0.25$. These parameters represent a flow similar to the experiment. In this particular case, upstream separation was first detected at $\Omega_0 = 0.839$ and preceded the fold at $\Omega_f = 0.866$. While the stream surfaces were almost undisturbed from the zero swirl case up to $\Omega = 0.754$,
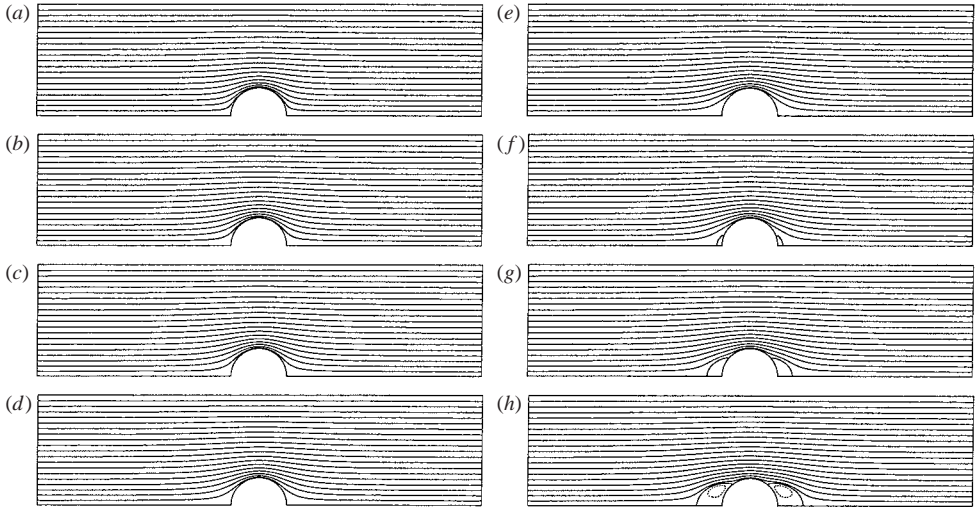
FIGURE 24. Stream surfaces for $\Omega =$ (a) 0, (b) 0.754, (c) 0.799, (d) 0.831, (e) 0.845, (f) 0.856, (g) 0.866 and (h) 0.845. Dashed lines indicate $\psi < 0$.
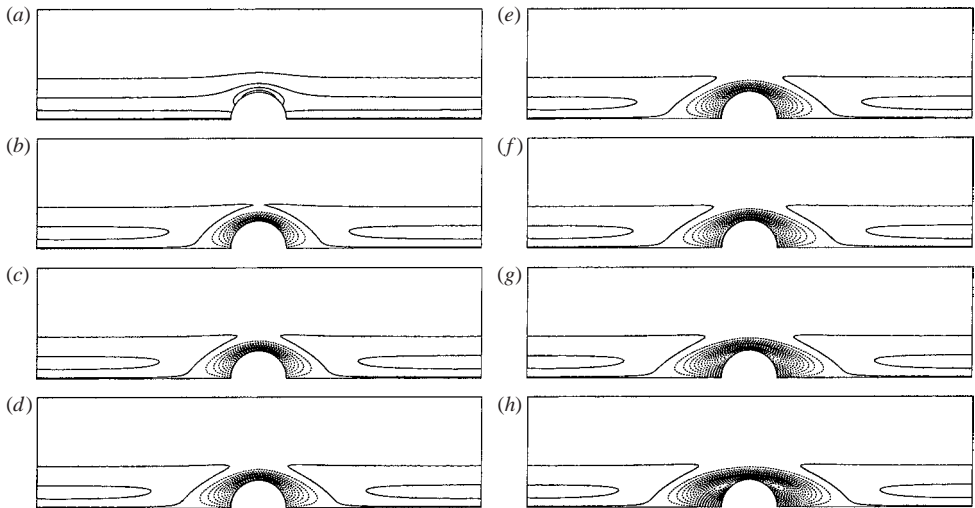

FIGURE 25. Isolines of $r_s\eta/W_0$ for $\Omega =$ (a) 0, (b) 0.754, (c) 0.799, (d) 0.831, (e) 0.845, (f) 0.856, (g) 0.866 and (h) 0.845. Isolines drawn at constant intervals in the range $[-3.80, 0.80]$. Dashed lines indicate $\eta < 0$.

significant changes to the azimuthal vorticity distribution occurred. At $\Omega = 0$ there is a positive azimuthal vorticity component upstream of the sphere which is associated with the axial velocity jet. Around the sphere, the azimuthal component increases. In this case, there is no axial vorticity and the vortex lines are rings centred on the axis of symmetry. As the flow expands around the sphere, the vortex lines are stretched and the azimuthal vorticity must increase. This has the effect of increasing the axial velocity component near the axis and is the reason why $-\partial w/\partial z$ increases as W_1/W_0 (and hence the azimuthal vorticity) is increased at zero swirl. As Ω is increased to 0.754, the behaviour of the azimuthal vorticity is reversed. The maximum azimuthal vorticity does not increase above the maximum value at the inlet and the azimuthal vorticity

β (deg.)	r_1/r_s	W_0/W_b	$(W_1 + W_0)/W_b$	r_0/R	W_1/W_0
16	0.78	1.11	1.34	0.183	0.207
19	0.80	1.05	1.36	0.188	0.295

TABLE 3. Flow properties at $z/r_s = -3.98$.

decreases and becomes negative as the flow diverges around the sphere. Between $\Omega = 0.754$ and $\Omega_0 = 0.856$, changes to the flow pattern occur much more rapidly. Increasing stream surface expansion, relative to the zero swirl case, upstream and downstream of the sphere is associated with axial growth of the negative azimuthal vorticity region and decreasing minimum azimuthal vorticity, eventually leading to upstream (and downstream) separation.

Out of interest, the results of analytic continuation beyond Ω_0 are also shown, bearing in mind the limitations discussed above. These show recirculation regions of slowly moving fluid on both upstream and downstream hemispheres. Note that there are two solutions at $\Omega = 0.845$. Figures 24(*e*) and 25(*e*) correspond to a solution before the fold, while figures 24(*h*) and 25(*h*) correspond to a solution after the fold. The final figure shows that the bubble grows as Ω decreases following the fold. For larger values of r_0/R, the qualitative behaviour following the fold begins to change. As the solution is continued, the upstream and downstream symmetry of the recirculation regions decreases, until a single bubble is located on either side of the sphere. This is the reason for the hooks in the solution paths evident in figures 22(*e*) and 22(*f*) (where the upstream bubble disappears).

A precise quantitative comparison between the numerical and physical experiments is complicated by a number of factors. First, the Q-vortex is not a completely accurate representation of the experimental vortex. Even if it was, the centreline axial velocity and, to a lesser extent, the core thickness depend on both Ω and z and hence $W_1/W_0 = f_1(\Omega, z/R)$ and $r_0/R = f_2(\Omega, z/R)$. These parameters were considered fixed during continuation and the solution paths therefore do not correctly represent the behaviour as Ω is increased in the experiment. In order to compute Ω_0, it is necessary to obtain the numerical values of W_1/W_0 and r_0/R from experimental data at Ω_0. Even if this swirl intensity could be accurately identified from the experiments (the numerical solutions suggest an explanation for this difficulty), the problem of which axial station best represents the properties of the undisturbed flow remains. Nevertheless, it can be demonstrated that the numerical solutions are not inconsistent with the experiments. Table 3 lists some properties of the flows at $\beta = 16°$ and $19°$ which were estimated from the first axial station in figures 6 and 7. Note that r_1 is the radius at which the peak azimuthal velocity occurs, which for the Q-vortex is related to r_0 by $r_1/r_0 = 1.121$; hence

$$\frac{r_0}{R} \approx \left(\frac{r_0}{r_1}\right) \left(\frac{r_1}{r_s}\right) \left(\frac{r_s}{R}\right) = \frac{0.263}{1.121} \frac{r_1}{r_s}.$$

W_0 is taken to be equivalent to the uniform axial velocity outside the pipe wall boundary layer and the vortex core. In the calculations it is assumed that the pipe wall boundary layer can be ignored and the axial velocity W_0 may be considered to extend to the pipe wall. The centreline axial velocity estimated from the experimental velocity profiles is assumed to be equivalent to the centreline axial velocity of the Q-vortex, $W_1 + W_0$. The ratio W_1/W_0 may then be determined from

$$\frac{W_1}{W_0} = \left[\frac{W_1 + W_0}{W_b} - \frac{W_0}{W_b}\right]\frac{W_b}{W_0}$$

and the modified swirl parameter may be estimated by multiplying the experimental value by W_b/W_0. Using average values of $r_0/R = 0.185$ and $W_1/W_0 = 0.25$, calculations on a 98×200 grid with $r_s/R = 0.263$ and $L/R = 4.0$ suggest $\Omega_0 = 0.74$, which is certainly in the correct range.

The numerical solutions suggest an explanation for the inconsistent behaviour which complicated the experiments. For parameters typical of the experiments, the solution fold and upstream separation occurred at similar values of Ω. Close to upstream separation, the flow is therefore very sensitive to small changes in Ω. This is reflected by the steep gradients of $-\partial w/\partial z$ close to Ω_0 in figure 22. Similarly, in figure 24 the stream surface pattern is almost unaffected up to $\Omega \approx 0.75$ after which dramatic variation, including upstream separation, occurs by increasing Ω by only 0.1. This corresponds to increasing β by only $2°$ in the experiments. It is therefore not surprising that the flow would be susceptible to small variations. The existence of a fold means that for some range of Ω there are at least two solutions. Folds are usually associated with a change in solution stability; hence if the solution on one side of the fold is stable, the other will be unstable. If it is assumed that the qualitative behaviour of solutions using analytic continuation for $\psi < 0$ is reflected by the physical flow, then this would explain why a stable separation bubble was possible for only a very limited range of Ω. Furthermore, if the divergence of the second unstable solution was sufficiently slow, then given certain initial conditions it might be possible to observe the unstable solution for a limited time. This would provide an explanation for the transient bubble at $\beta = 16°$.

6. Conclusion

For concentrated vortex flow past a sphere in a pipe, the initial effect of swirl is to shorten the downstream separation bubble. For a small range of Ω, it is possible for an almost stagnant upstream separation bubble to exist. The bubble becomes unstable at larger values of Ω and the flow subsequently becomes unsteady and three-dimensional. At sufficiently large Ω the downstream separation is eliminated and an unsteady, three-dimensional disturbance penetrates far upstream.

Analysis of experimental data and numerical solutions of steady inviscid axisymmetric flow suggest that upstream separation is caused by the distortion of vortex lines in the diverging flow approaching the sphere as originally suggested by Brown & Lopez (1990).

For parameters typical of the experiment, a solution fold is found in the vicinity of upstream separation. In this regime, the flow is very sensitive to changes in Ω. It is suggested that this accounts for the extreme sensitivity encountered in the experiments.

REFERENCES

ALTHAUS, W., BRÜCKER, CH. & WEIMER, M. 1995 Breakdown of slender vortices. In *Fluid Vortices*. Kluwer ed.

BATCHELOR, G. K. 1967 *An Introduction to Fluid Dynamics*. Cambridge University Press.

BENJAMIN, T. B. 1962 Theory of the vortex breakdown phenomena. *J. Fluid Mech.* **14**, 593–629.

BERAN, P. S. & CULICK, F. E. C. 1992 The role of non-uniqueness in the development of vortex breakdown in tubes. *J. Fluid Mech.* **242**, 491–527.

BROWN, G. L. & LOPEZ, J. M. 1990 Axisymmetric vortex breakdown. Part 2. Physical mechanisms. *J. Fluid Mech.* **221**, 553–576.

BRÜCKER, C. & ALTHAUS, W. 1995 Study of vortex breakdown by particle tracking velocimetry (PTV). Part 3: Time-dependent structure and development of breakdown-modes. *Exps. Fluids* **18**, 174–186.

BUNTINE, J. D. & SAFFMAN, P. G. 1995 Inviscid swirling flows and vortex breakdown. *Proc. R. Soc. Lond.* A **449**, 139–153.

ESCUDIER, M. P. 1988 Vortex breakdown: Observations and explanations. *Prog. Aerospace Sci.* **25**, 185–229.

ESCUDIER, M. P. & KELLER, J. J. 1985 Recirculation in swirling flow: A manifestation of vortex breakdown. *AIAA J.* **23**, 111–116.

FALER, J. H. & LEIBOVICH, S. 1978 An experimental map of the internal structure of a vortex breakdown. *J. Fluid Mech.* **86**, 313–335.

JOUBERT, P. N. & WANG, M. H. 1987 Drag on a sphere in swirling flow. In *Sixth Sympo. on Turbulent Shear Flows, Paul Sabatier University, Toulouse, France*.

JOUBERT, P. N. & WANG, M. H. 1989 Lift on a grounded sphere under a tornado vortex. In *Seventh Symp. on Turbulent Shear Flows, Stanford University, California, USA*.

JOUBERT, P. N. & WANG, M. H. 1992 LDA measurements of the flow field about an isolated sphere in swirling flow. In *Sixth Intl Symp on Applications of Laser Techniques to Fluid Mechanics, Lisbon, Portugal*.

KIM, I., ELGHOBASHI, S. & SIRIGNANO, A. 1995 Unsteady flow interactions between an advected cylindrical vortex tube and a spherical particle. *J. Fluid Mech.* **288**, 123–155.

LEIBOVICH, S. 1984 Vortex stability and breakdown: Survey and extension. *AIAA J.* **22**, 1192–1206.

LEIBOVICH, S. & KRIBUS, A. 1990 Large-amplitude wavetrains and solitary waves in vortices. *J. Fluid Mech.* **216**, 459–504.

LONG, R. R. 1953 Steady motion around a symmetrical obstacle moving along the axis of a rotating liquid. *J. Met.* **10**, 197–203.

MATTNER, T. W. 2000 Vortical flow past a sphere. PhD thesis, University of Melbourne.

MATTNER, T. W., JOUBERT, P. N. & CHONG, M. S. 2002 Vortical flow. Part 1. Flow through a constant diameter pipe. *J. Fluid Mech.* **463**, 259–291.

MAXWORTHY, T. 1970 The flow created by a sphere moving along the axis of a rotating, slightly-viscous fluid. *J. Fluid Mech.* **40**, 453–479.

MILES, J. W. 1971 Boundary-layer separation on a sphere in a rotating flow. *J. Fluid Mech.* **45**, 513–526.

MITÁSŎVÁ, H. & MITÁŠ, L. 1993 Interpolation by regularized spline with tension: I. Theory and implementation. *Math. Geol.* **25**, 641–655.

MITÁSŎVÁ, H., MITÁŠ, L., BROWN, W. M., GERDES, D. P., KOSINOVSKY, I. & BAKER, T. 1995 Modelling spatially and temporally distributed phenomena: new methods for GRASS GIS. *Intl J. Geograph. Informat. Syst.* **9**, 433–446.

PANCHAPAKESAN, N. R., MATTNER, T. W., CHONG, M. S. & JOUBERT, P. N. 1995 LDV measurements in a swirling vortex flow around a sphere. In *Twelfth Australasian Fluid Mechanics Conf.* (ed. R. W. Bilger), vol. 2, pp. 675–678. The University of Sydney.

PROUDMAN, J. 1916 On the motion of solids in liquids possessing vorticity. *Proc. R. Soc. Lond.* A **92**, 408–424.

ROCKWELL, D. 1998 Vortex-body interactions. *Annu. Rev. Fluid Mech.* **30**, 199–229.

RUSAK, Z. 1996 Axisymmetric swirling flow around a vortex breakdown point. *J. Fluid Mech.* **323**, 79–105.

RUSAK, Z., JUDD, K. P. & WANG, S. 1997 The effect of small pipe divergence on near critical swirling flows. *Phys. Fluids* **9**, 2273–2285.

RUSAK, Z., WANG, S. & WHITING, C. H. 1998a The evolution of a perturbed vortex in a pipe to axisymmetric vortex breakdown. *J. Fluid Mech.* **366**, 211–237.

RUSAK, Z., WHITING, C. H. & WANG, S. 1998b Axisymmetric breakdown of a Q-vortex in a pipe. *Phys. Fluids* **36**, 1848–1853.

SNYDER, D. E. & SPALL, R. E. 2000 Numerical simulation of bubble-type vortex breakdown within a tube-and-vane apparatus. *Phys. Fluids* **12**, 603–608.

TAYLOR, G. I. 1917 Motion of solids in fluids when the flow is not irrotational. *Proc. R. Soc. Lond.* A **93**, 99–113.

TOMBOULIDES, A. G. & ORSZAG, A. A. 2000 Numerical investigation of transitional and weak turbulent flow past a sphere. *J. Fluid Mech.* **416**, 45–73.

WANG, S. & RUSAK, Z. 1997a The effect of slight viscosity on a near-critical swirling flow in a pipe. *Phys. Fluids* **9**, 1914–1927.

WANG, S. & RUSAK, Z. 1997b The dynamics of a swirling flow in a pipe and transition to axisymmetric vortex breakdown. *J. Fluid Mech.* **340**, 177–223.